Design and fabrication of a measurement system for braking rheostat losses

Samriddh Sharma

Design and fabrication of a measurement system for braking rheostat losses

A thesis submitted to the Delft University of Technology in partial fulfillment of the requirements for the degree of

Master of Science in Electrical Power Engineering

by

Samriddh Sharma

Student number: 4796667

Intelligent Electrical Power Grids (IEPG)
Department of Electrical Sustainable Energy
Faculty of Electrical Engineering, Mathematics and Computer Science
Delft University of Technology

Supervisors:

University Supervisor:	Dr. ir. Marjan (M.) Popov	Delft University of Technology
Company Supervisor:	Dr. Helko (H.E.) van den Brom	Van Swinden Laboratory

Thesis Committee

Dr. ir. Marjan (M.) Popov	Associate Professor	Delft University of Technology
Prof. dr. Peter (P.) Palensky	Full Professor	Delft University of Technology
Dr. Armando (A.) Rodrigo Mor	Assistant Professor	Delft University of Technology
Dr. Helko (H.E.) van den Brom	Principal Scientist	Van Swinden Laboratory

An electronic version of this dissertation is available at
http://repository.tudelft.nl/.

Arise awake and stop not until the goal is achieved.

Swami Vivekananda

Contents

Summary

In the World Energy Outlook (2019), the International Energy Agency (IEA) estimates the growth of global energy demand by 1.3% every year until 2040 in the existing policy scenario. Today the world is not on track to meet the energy-related components of the Sustainable Development Goals (SDGs) set down by the United Nations General Assembly (UNGA) in 2015.

Today, 60% of the European mainline railway network is electrified with 80% of total traffic. It will further increase driven by The Trans-European Transport Network (TEN-T) and sustainability initiatives. As electricity consumption by railway networks increases, quantification of rail transport's actual energy consumption is essential. Currently, railways' energy consumption is measured at the supply side, i.e., the grid, which includes the network's losses. This measurement does not give actual energy consumption. The European Union demanded an on-board energy measurement system for railways from 2019 onward.

The existing energy measurement systems designed for transmission and distribution networks are not suitable for railway applications due to the harsh conditions. The voltage and current signals are highly distorted and need a more sophisticated measurement system. The energy measurement can be divided into current measurement, voltage measurement, and energy calculation. This thesis project is part of the ongoing research in the current measurement for the on-board energy measurement system focusing on the DC current measurement.

The primary objective is to measure the energy dissipated during braking of the train. Therefore, we need to measure the current flowing through the braking rheostat during the braking of the train. This current measurement is difficult due to the fast switching of high current (in order of 500 A-600 A) termed as chopped current.

VSL has developed a test setup to measure the chopped current flowing through the braking rheostat. The test setup must be modified to achieve the project requirement of 600 A current measurement and test chopped waveform signals for calibration of the current measurement system. Intermediate tests were performed during the modification of the test setup to analyze the components' performance. Finally, the modified setup is tested up to load current of 600 A, and uncertainty calculation performed on the measurement results.

Acknowledgments

My thesis project with Van Swinden Laboratory (VSL), Delft, gave me an excellent learning and professional development opportunity. I am fortunate to get the chance to be a part of such a wonderful organization. I am delighted to have met many wonderful people and professionals who led me through this project period.

Firstly, I would like to thank Professor Peter Palensky for his vision and constant support to impart practical knowledge to Electrical Power Engineering students. I appreciate the encouragement from Dr. Marjan Popov, my university supervisor, for providing me a chance to work with the industry in the form of this thesis project.

I want to express my gratitude towards the staff and employees of VSL, Delft, for their time, effort, and support they showered on me during this project. I am highly indebted to Dr. Helko E. van den Brom for his guidance and constant supervision. I sincerely thank Ms. Lydia for her help and support during my time at VSL.

My special thanks to Dr. Ronald van Leeuwen for his constant cooperation and support during my project period. I also thank Zander Marais and Jan van der Beek to provide me with the necessary help required for this project. I would also like to thank Henk Ulden for his help and expertise during the setup modification. I am also grateful to Drs. Fabienne van Bomma, Dr. Marc Pieksma, and Dr. Marjin van Veghel for giving me this opportunity at VSL and their encouragement and the constant guidance in completing this project.

My thanks and appreciation also go to my university, colleagues, parents, friends, and fellow students for being there for me during this project.

Samriddh Sharma
Delft, September 2020

List of Figures

List of Tables

1

Introduction

If you cannot measure it,
you cannot improve it

William Thomson, 1st Baron Kelvin

Rail transport is one of the most efficient, economic, and environmentally friendly means of mass transport. The rail industry in the EU has grown 1.2% every year since 1995 [1] due to an increase in population, GDP, technological advancement, globalization, digitization, and commitment for safe travel. Today, the European Union is a close-knit politico-economic community with 28 member states and five potential candidates. The European Single Market provides a platform for free movement of goods, capital, services, and labor. The energy market and transportation are the base for this free movement, and the rail transport networks play a crucial role in it.

The European railway system is one of Europe's largest energy consumers with approximate annual consumption of 36.5 TWH [2]. With an ambitious target to reduce CO_2 railway transport emissions by 50% by 2030 and to establish a single European railway network, the European Union requires an efficient energy measurement system to calculate energy billing based on the actual energy consumption by railways. Single European Railway Directive 2012/34/EU and subsequent Railway Packages set a group of European Union legislations aiming towards enabling a single pan-European Railway network for passenger and freight transport [3]. One essential part of this is establishing an energy measurement protocol that would enable accurate and actual energy measurement.

The proposed on-board Energy Measurement System (EMS) (1.1) is based on the requirement of EN 50463-2, which states that all trains shall be equipped with an Energy Measurement Function (EMF), whose measurement accuracy should be

1

assessed and periodically re-verified [4]. Energy Measurement Function (EMF) consists of 3 functions- a. Current Measurement Function, b. Voltage Measurement Function, and c. Energy Calculation Function. The calculated energy is sent to an on-ground Data Collection Service (DCS) via a Data Handling System (DHS).

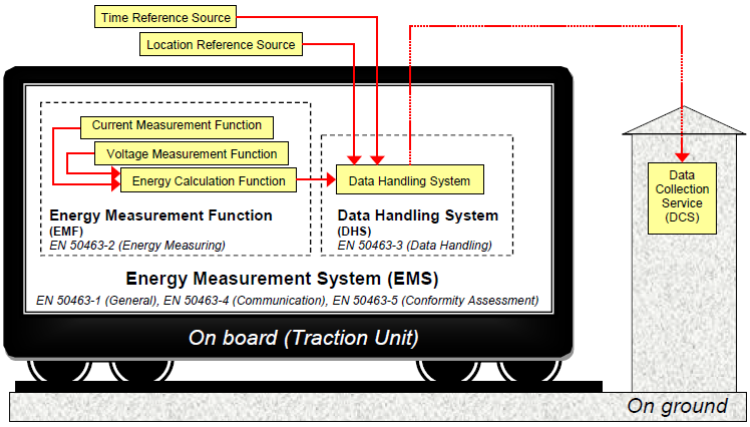

Figure 1.1: Energy Measurement System (EMS) for on-board trains

The MyRailS Project (16ENG04) was commissioned under the European Metrology Programme for Innovation and Research (EMPIR) initiative, co-funded by the European Union's Horizon 2020 research and innovation program and EMPIR participating members, under EURAMET - The European Association of National Metrology Institutes. The consortium of 7 National Metrology Institutes (NMIs), 3 Universities, and 6 Companies jointly working together to develop the metrological framework and measurement infrastructure that will drive the implementation of energy-efficient technologies in European railway systems. This thesis is part of one of the EMS sub-systems - the Current Measurement Function (CMF). The thesis project aimed to establish a calibration protocol for braking rheostat losses in railways during braking.

1.1. Problem statement

An error of 5% on 36.5 TWh of energy consumption by European Railways equates to a value of 110M Euros each year. For a precise and reliable measurement of the energy transfer between the train and the grid, a new on-board measurement system needs to be established. This on-board measurement system should be suitable for much severe and dynamic conditions than the conventional transmission and distribution networks.

One of the five objective of the MyRailS project is to develop a metrological framework for calibrations (comprising of laboratory and on-board train calibration/measurement setups and robust data processing algorithms) to enable high accuracy energy and Power Quality (PQ) measurements under highly dynamic elec-

trical conditions approaching the uncertainty limits stated in the EN 50463-2:2013-05 [2].

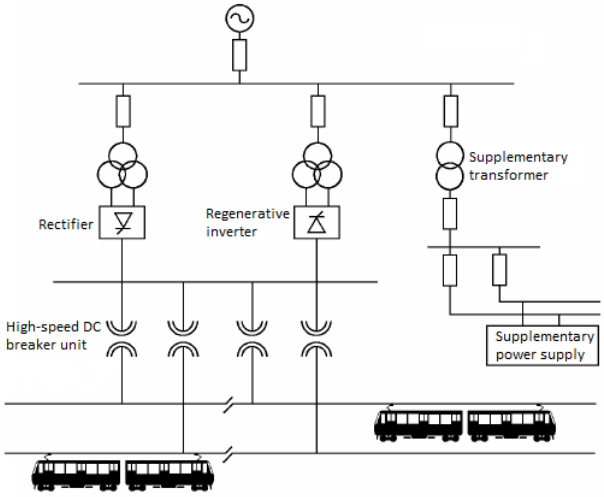

Figure 1.2: On-ground power system connection to electrified rail

The European railway traction power supply system consists of AC and DC networks. This thesis project focuses on the DC traction networks (3 kV and 1.5 kV). A ground substation has an AC-DC converter (Rectifier), which provides DC power to the Overhead line (1.2) [5]. A metallic arm mounted on the roof of the train makes contact with the overhead lines. An on-board inverter converts the DC power to AC power for traction and auxiliary consumption. During braking, the traction motors act as generators. This regenerated power is transferred to the DC grid of the train. When the braking energy is sent back to the grid, it is termed as regenerated braking. When the braking energy is transferred to the braking rheostat, it is termed as rheostat braking. The current I_{br} (1.3) during rheostatic braking needs to be measured in order to calculate the braking energy.

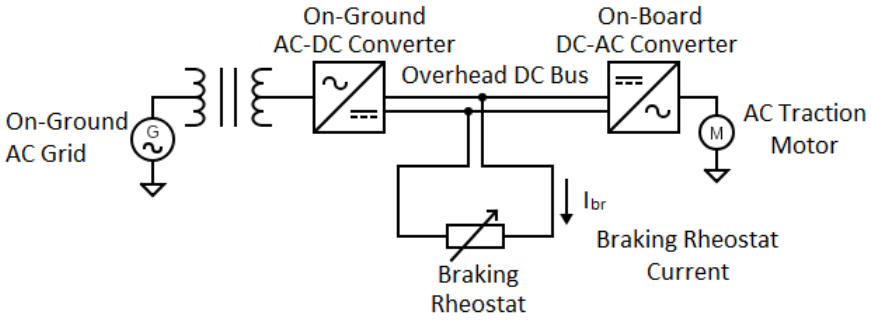

Figure 1.3: Simplified schematic of the traction power system

1

VSL is responsible for developing two setups for calibration of AC and DC energy measurement systems, including uncertainty estimation. This thesis is part of the calibration setup for DC measurement of braking rheostat current. The measurement of braking rheostat current is difficult due to the fast switching characteristics. A special current transformer for DC measurement termed as DC-current transformer (DCCT) is used. In the initial measurement setup developed at VSL [6–8], it was concluded that the system's active components lead to distortion during turn-on and turn-off in the braking rheostat current. This thesis's problem statement is derived from these observations of distortions, and a modified setup was proposed, build, and tested.

This thesis's primary objective is to modify the existing setup developed by VSL for calibration of braking rheostat current. The existing setup is comprised of a high-power DC current source and a programmable DC electronic load. The distortion observed during switching in case of the chopped waveform is to be eliminated. This distortion is due to the electronic component of the power source and the programmable load. It was proposed to make the programmable load as a passive component in the circuit. Based on this proposal, the following research questions (RQ) are listed, which we will seek answers to:

RQ 1: How can the programmable DC electronic load be made a passive element?

RQ 2: How to extend the setup to 600 A in order to meet the project requirement?

RQ 3: How can we evaluate the effect of slew rate in the chopped waveform for passive behavior of programmable DC electronic load?

RQ 4: What would be the uncertainty in the measurement of braking rheostat current?

1.2. Approach

The intention behind **RQ 1** is to eliminate the distortion caused by the interaction between the electronic components present in the high-power DC current source and programmable DC electronic load. As we focus on the current measurement system, the system's voltage is intentionally kept low, and the current is extended to the limits.

RQ 2 is the next step to achieve the higher current limit, as agreed in the project proposal. Since electronic load has a 600 A capacity, the modified circuit should take care of a higher current up to 900 A. It was proposed to limit the current of 600 A in the programmable load path and propose an alternate path for the remaining 300 A.

In the case of the existing test setup developed by VSL, slew rate play an essential role in distortion. To investigate this effect in case of passive behavior of the programmable load would be essential for the calibration setup's accuracy and traceability. **RQ 3** is essential to establish the measurement setup.

In metrology, measurement uncertainty is a crucial parameter. All measurements have uncertainty, and measurement results are incomplete without the associated uncertainty. **RQ 4** is a significant metrology aspect of the project and

would be calculated based on the dispersion of measurement values in the modified setup.

1.3. Thesis outline

The following chapters of the thesis are organized according to the setup requirements. Chapter 2 covers the train's electrical system, braking, and measurement system being used in the setup. The initial and revised setups are explained in Chapter 3, which covers further tests to establish the distortion effect. Based on the initial setup observation, Chapter 4 covers the design steps of setup modification and tests performed. Finally, in Chapter 5, we establish the tests' results with the modified setup and compare the initial setup results. The uncertainty measurement would also be accomplished along with the measurement. Finally, Chapter 6 includes the conclusion of the thesis and the future work that would be performed by VSL to establish the setup for the MyRailS project.

References

[1] European Commission and Directorate General for Mobility and Transport, *EU transport in figures: statistical pocketbook 2019.*, OCLC: 1127847098.

[2] EURAMET-European Association of National Metrology Institutes, *Publishable Summary: Metrology for smart energy management in electric railway systems (MyRailS 16ENG04),* (2020).

[3] European Parliament, *Directive 2012/34/EU establishing a single european railway area,* (2012).

[4] CENELEC - Standards Development, *Railway applications - energy measurement on board trains - part 2: Energy measuring,* (2012).

[5] L. Liudvinavičius and L. P. Lingaitis, *Electrodynamic braking in high-speed rail transport,* in *Transport 2007*.

[6] H. E. van den Brom, R. van Leeuwen, and R. Hornecker, *Characterization of DC current sensors under distorted conditions for railway applications,* in *2018 IEEE International Conference on Electrical Systems for Aircraft, Railway, Ship Propulsion and Road Vehicles & International Transportation Electrification Conference (ESARS-ITEC)* (IEEE) pp. 1–6.

[7] H. E. van den Brom, R. van Leeuwen, and R. Homecker, *Characterization of a reference DC current transducer with AC distortion for railway applications,* in *2018 Conference on Precision Electromagnetic Measurements (CPEM 2018)* (IEEE) pp. 1–2.

[8] H. E. van den Brom, R. van Leeuwen, and R. Hornecker, *Characterization of DC current sensors with AC distortion for railway applications,* in *IEEE Transactions on Instrumentation and Measurement*, Vol. 68, pp. 2084–2090.

2

Electrical system of a train

Most of modern trains use electricity as the source of energy for traction. The traction power supply can be AC or DC (25 kV/50 Hz, 15 kV/16.7 Hz, 3 kV/DC, 1.5 kV/DC, 750 V/DC, and 600 V/DC). The on-ground power supply is connected to a moving train either through an overhead line or a third rail. The overhead line used for traction power supply is called a catenary. A protruding arm, mounted over the train called a pantograph, makes sliding contact with the catenary. The electrical system's major components in the train remain the same irrespective of the type of connection.

2.1. AC and DC locomotive

The AC locomotive consists of a main transformer and the main rectifier (AC-DC converter) that feeds the DC-grid of the locomotive (DC-link). An auxiliary inverter (DC-AC converter) is used for lighting, air-conditioning, and other electrical systems. The traction inverter (DC-AC converter) provides an AC connection for traction motors (3-phase AC motors). The braking unit consists of a braking rheostat and a chopper unit.

The DC locomotive is the same as the AC locomotive from the DC-link. It also consists of auxiliary and traction inverter. Similar to AC locomotive, 3-phase AC motors are used for traction. The braking unit is employed during braking.

2.2. Braking

There are two braking mechanisms in the locomotive; mechanical and dynamic braking. The mechanical braking is used mainly for low-speed braking like stopping at stations. It is not designed for high-speed braking; used only in case of emergency braking [1, 2]. The dynamic braking uses the electrical properties of the traction motor. When a brake is applied, the motor acts as a generator. The generated electrical energy is fed back to the overhead line called the regenerative

braking. Furthermore, if the line voltage of the overhead line exceeds the voltage limit, the excess energy is fed to braking rheostat termed as the rheostatic braking.

2.2.1. Regenerative braking

A small portion of the recovered electrical energy is reused to power vehicles auxiliaries, whereas the remaining energy is re-injected to the grid by reversible substations (2.1). Since most of the existing substations are unidirectional, the recovered energy has to be utilized by an accelerating vehicle nearby (2.2) [3]. The remaining unused energy or all the recovered energy in case of no accelerating vehicle nearby; is dissipated through braking rheostat. Regenerative braking is considered an energy-efficient and cost-effective method as the power regenerated by the train is either used by another train nearby or returned to the network.

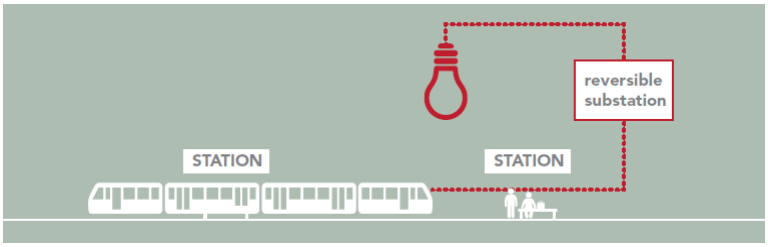

Figure 2.1: Concept of reversible substation in a rail network

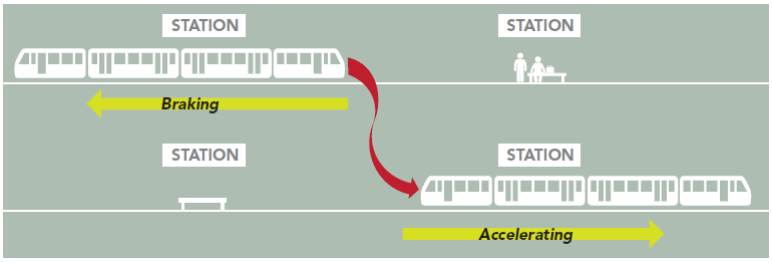

Figure 2.2: Concept of regenerative braking on a rail network

2.2.2. Rheostatic braking

When the regenerated energy is fed back to the grid, if the voltage exceeds the specific limit, the energy is dissipated through a rheostat called a braking rheostat [4]. The continuous current needs to be chopped using a chopper circuit to limit the braking rheostat's power dissipation and excess heating.

2.3. Chopped waveform

The current through the braking rheostat has fast on/off switching and is characterized as "Chopped Waveform". The measurement setup for the calibration should

generate this fast switching action, and the reference sensor should be capable of following it [5]. For an accurate measurement, current measurement should follow this fast switching. Slew rate is defined as a change in voltage or current per unit time. For a square wave, the slew rate is infinity, whereas, for a chopped wave, the slew rate can be defined. The slew rate for the chopped waveform in example graph (2.3) is 10 $A/\mu s$.

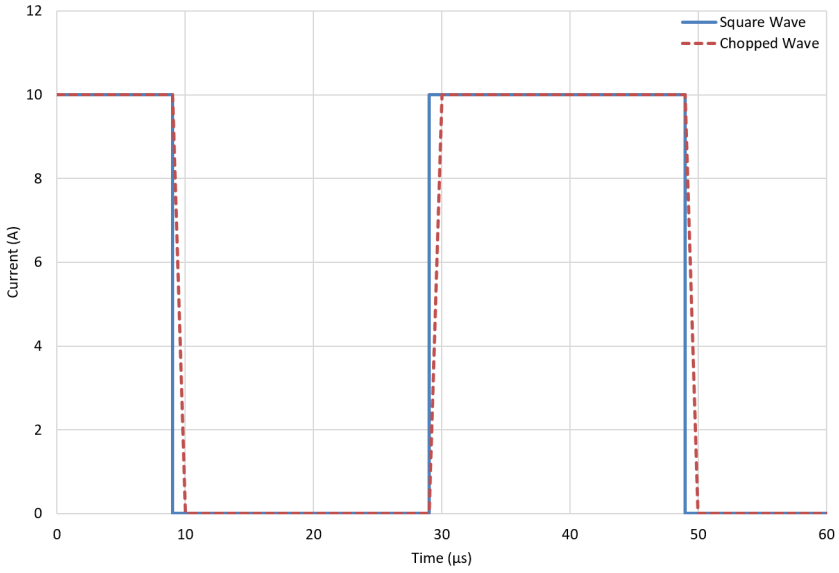

Figure 2.3: An example of a square and chopped waveform of 10 A

This thesis focuses on the measurement of energy dissipated in braking rheostat during braking. And to calculate the energy, current through the braking rheostat and voltage across it is to be measured. Here, we are working on the chopped current measurement.

A virtual power source will be used here instead of real power to reduce energy dissipation during calibration and testing. This virtual power, termed as phantom-power, consists of two separate current and voltage loops. For current measurement, low voltage and the required current is applied. Whereas, for voltage measurement, low current and the required voltage is applied. Some phantom-power generation methods have high accuracy and can attain higher voltage and current generation levels, but they are designed primarily for power frequency. Another setup is being developed as part of the MyRailS project, which is unique, generating voltage and current even at higher frequencies [6].

The current through the braking rheostat needs to be measured for testing and calibration purposes during regenerative braking action. For this current measurement, voltage is not essential, so a new power source needs to be implemented, which would deliver the required current. This approach of using only the current source is part of phantom power.

2.4. Current measurement

Current measurement is a critical task is high-performance power applications, tests, and measurement setup, including a calibration system. The type of current sensors available are listed in 2.1.

Type	AC	DC	I-I	I-V	Invasive
CT	✓	✗	✓	✗	✗
Zero-flux	✓	✓	✓	✓	✗
Shunt	✓	✓	✗	✓	✓
Hall-effect	✓	✓	✗	✓	✗
Rogowski	✓	✗	✗	✓	✗

Table 2.1: Types of current sensors

A shunt resistor is not preferred to measure the chopped current measurement as this invasive technique is not isolated from the conductor to be measured. Hall effect sensor is not suitable because of high-temperature dependency up to 152 mV/VT, poor linearity, and reduced precision [7]. Therefore, a zero-flux current sensor is the most suitable current measurement technique for accurate and reliable measurement of braking rheostat current.

Zero-flux current measurement

The current transformer (CT) is widely used for measuring AC, which cannot measure low-frequency AC or DC. The presence of DC in the transformer saturates the magnetic field (S_1S_2) in the core, which is outside the typical linear region(OS_1) in the B-H curve (2.4). So, Direct Current-Current Transformer (DCCT), based on the zero-flux principle, measures low-frequency AC and DC with high accuracy. Zero-flux can be capable of measuring AC and DC.

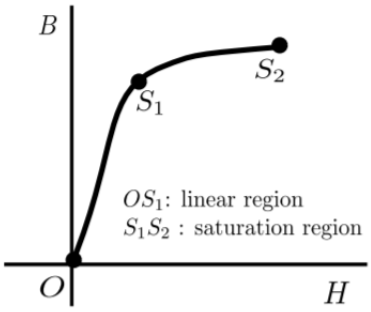

Figure 2.4: DC magnetization curve

Basic principle

To deal with the saturation of the core, we place a secondary winding on the core. The current applied to the secondary winding is opposite to the primary current.

This brings the core back to the linear region. A third small AC current is applied, generating secondary harmonic peaks in the saturation region. These peaks are detected using a peak detector. The applied secondary current will be proportional to these peaks. The secondary harmonic peaks do not occur in the linear region.

Working

The primary current (Ip), which is to be measured, generates a magnetic flux that is canceled by the flux generated by the secondary current (Is) [8]. The remaining flux is sensed by three-toroidal wound ring cores located within the secondary winding. Two of these rings (N1 and N2) senses the DC component of the remaining flux, and N3 senses the AC component. The oscillator connected to the two DC flux sensing cores saturates them in the opposite direction. If the DC flux is zero, the resulting current peaks are equal in both directions. If not zero, the difference of the current peak is proportional to the residual DC flux. AC component (N3) is added, and a control loop is set up to generate the secondary current, which makes the DC flux zero. The secondary current (Is) is 1/Ns times the primary current is provided by a power amplifier to the secondary winding. The secondary current (Is) fed to the burden resistor converts the signal into a voltage, amplified by a precision amplifier (2.5).

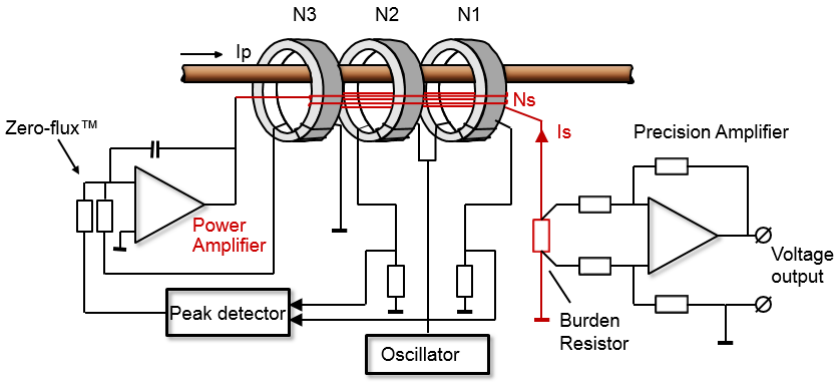

Figure 2.5: Schematic depicting Zero-flux principle

Above several kHz, the power amplifier no longer has active control over its output current but merely forms a short circuit. The bandwidth of zero-flux CT is only limited by stray reactance and capacitance in the head and interconnecting cables. For zero-flux CT with current output, the secondary current is the output. Here, the burden resistor and precision amplifier are omitted.

In the case of core saturation due to primary current overload, the zero-flux condition is lost, and a next search cycle is automatically started. The secondary current varies between minus and plus current limit until zero-flux is detected.

Burden resistor

For precision measurement, a four-wire resistor is used. The low resistance of the burden resistor leads to the low voltage drop at rated current, which keeps the power dissipation low. The burden resistor has high thermal stability under normal load conditions to ensure precise measurement. Here, we are using a calibrated high-precision shunt as the burden resistor. The secondary current is measured directly using the shunt and a multi-meter eliminating the precision amplifier.

References

[1] G. Crotti, D. Giordano, D. Signorino, A. D. Femine, D. Gallo, C. Landi, M. Luiso, A. Biancucci, and L. Donadio, *Monitoring energy and power quality on board train,* in *2019 IEEE 10th International Workshop on Applied Measurements for Power Systems (AMPS)*, pp. 1–6, ISSN: 2475-2304.

[2] G. Cipolletta, A. D. Femine, D. Gallo, C. Landi, M. Luiso, A. Gallo, L. Pastena, F. Balic, J. Q. Fernández, D. Giordano, and D. Signorino, *Monitoring a DC train supplied by a reversible substation,* in *2020 IEEE International Instrumentation and Measurement Technology Conference (I2MTC)*, pp. 1–6, ISSN: 2642-2077.

[3] Ticket to Kyoto project (2010- 2014), *Final Report: Ticket to Kyoto*.

[4] L. Liudvinavičius and L. P. Lingaitis, *Electrodynamic braking in high-speed rail transport,* in *Transport 2007*.

[5] H. van den Brom and R. van Leeuwen, *Calibrating sensors to measure braking chopper currents in DC traction units,* in *2020 Conference on Precision Electromagnetic Measurements (CPEM)* (IEEE) pp. 1–2.

[6] D. Signorino, G. Crotti, A. D. Femine, D. Gallo, D. Giordano, C. Landi, and M. Luiso, *Phantom power generator for DC railway metrology,* in *2019 IEEE International Instrumentation and Measurement Technology Conference (I2MTC)* (IEEE) pp. 1–5.

[7] I. N. Cholakova, T. B. Takov, R. T. Tsankov, and N. Simonne, *Temperature influence on hall effect sensors characteristics,* in *2012 20th Telecommunications Forum (TELFOR)*, pp. 967–970.

[8] PM Special Measuring Systems B.V., *The basic principle of zero-flux,* .

3

Previous setups and tests

The current sensors readily available in the market have a specific operating range and associated accuracy as given by the manufacturers. These operating conditions are based on distortion-free signals within a specific temperature range. For calibration and accurate measurement, a system to be implemented should be capable of handling dynamic signals recorded in non-ideal conditions. VSL developed a new measurement setup to calibrate the current sensors under realistic conditions.

Initially, a current sensor is used as a reference for calibrating the other current sensor termed as a device under test (DUT). The DUT here, the zero-flux current sensor is calibrated, and AC distortion has no significant effect (few parts per 10^6) [1]. Next, the measurement setup is revised, and the zero-flux current sensor is taken as a reference for the next DUT (a high-current shunt resistor) [2].

Some measurement systems already exist for measuring the highly distorted signals for ac or dc high-current applications. However, they lack the traceability to international standards. The measurement setup, which can establish traceability to international standards were only suitable for static signals.

3.1. Test for comparison of two current sensors

Initially, the LEM ITN 900-S Ultrastab zero-flux current sensor (3.1) is taken as a reference device. The device under test (DUT) is the LEM IT 60-S Ultrastab zero-flux current sensor. The DC primary current is supplied by a 100 A DC current source on the two devices' primary windings. The AC signal is applied by a separate winding through the reference zero-flux current sensor to verify that the AC distortion does not affect the ITN 900-S zero-flux current sensor. The 900 A zero-flux current sensor is connected to a 1 A (R_{S1}) current shunt and 60 A zero-flux current sensor is connected to a 100 mA (R_{S2}) current shunt (3.2). The voltage across the current shunt is measured using two digital voltmeters (DVMs) Agilent 3458A [1–3].

The conversion ratio of LEM IT 60-S Ultrastab is 1:600 and the current ratio of

Figure 3.1: LEM ITN 900-S Ultrastab zero-flux current sensors

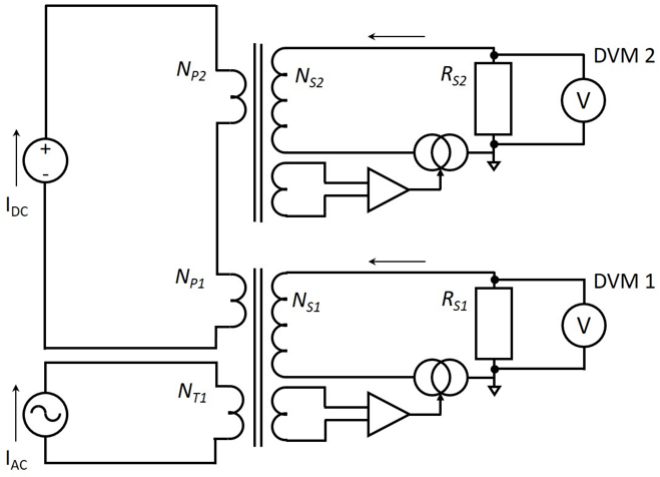

Figure 3.2: Schematic of the measurement setup to compare two current sensors

LEM ITN 900-S Ultrastab is 1:1500. So, the measured current is defined as follows:

$$\text{Measured Current } (I_p) = \frac{\text{Measured Voltage}}{R_{\text{shunt}}} \times \frac{\text{Conversion Ratio}}{\text{Number of turns}}$$

During the test for static signal by VSL, it was concluded that AC distortion on DC output reading of reference current sensor is within five parts in 10^6 [1]. For the test of dynamic signals, the test setup was revised by VSL, which is explained in the following section.

3.2. Test for characterization of DC shunt current sensor

To test the dynamic signals, the initial setup was revised, and the programmable DC electronic load Z_{load} was connected in series with the high-power DC current source (3.3). The high-power DC current source (Magma Power TS A5-900/415 rated for 5V/900) provides DC primary current I_p. The primary current is modulated using a programmable DC electronic load Z_{load} (Chroma 63206A-150-600 rated for 0-150 V, 0-600 A). The electronic load can be programmed to simulate various load profiles with uni-polar currents up to 600 A with frequency components up to 20 kHz. The LEM ITN 900-S zero-flux current sensor is used here as the reference along with a 1 A (R_{aux}) current shunt. The DUT here is the high-current Ohm Labs multiple current shunt (R_{dut}) of nominally 100 $\mu\Omega$, designed for operation for currents up to 300 A and equipped with an active cooling fan.

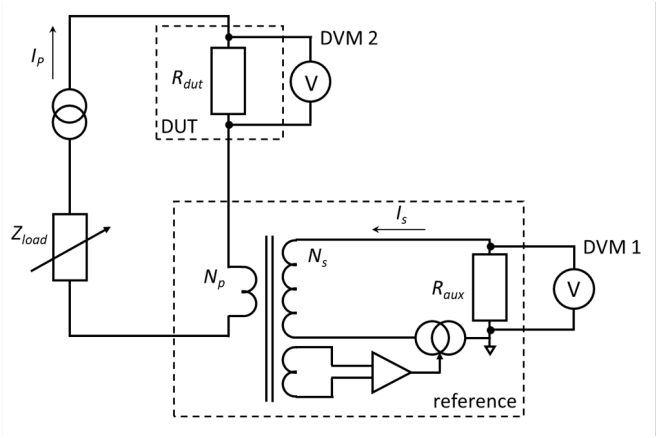

Figure 3.3: Schematic of the measurement setup to characterize a DC shunt current sensor

Various tests and measurements were performed by VSL to isolate the influence of the stability of the shunt, intrinsic current dependence, response to dynamic loading, and the effect of AC distortion [1–3]. The drift observed in the case of the shunt was considered to be the result of self-heating. It was further concluded that error increases with decreasing current. Some additional tests were performed using the chopped waveform, which is covered in the following sections.

3.3. Chopped waveform in revised test setup

The chopped waveform is the applied signal, i.e., the input current to be measured by the revised test setup (3.3). The current is measured using the high-current shunt and zero-flux current sensors. Various tests were performed by changing the parameters of the input chopped waveform.

3.3.1. Shunt and zero-flux current measurement

A 40 A input current is applied from the high-power current source. This current is measured by the current sensors present in the circuit: high-current shunt and zero-flux current sensor. It was observed (3.4) that the zero-flux is a more accurate and stable transducer than a shunt. In the measurement by the current shunt, a significant positive current spike and a negative current spike are observed.

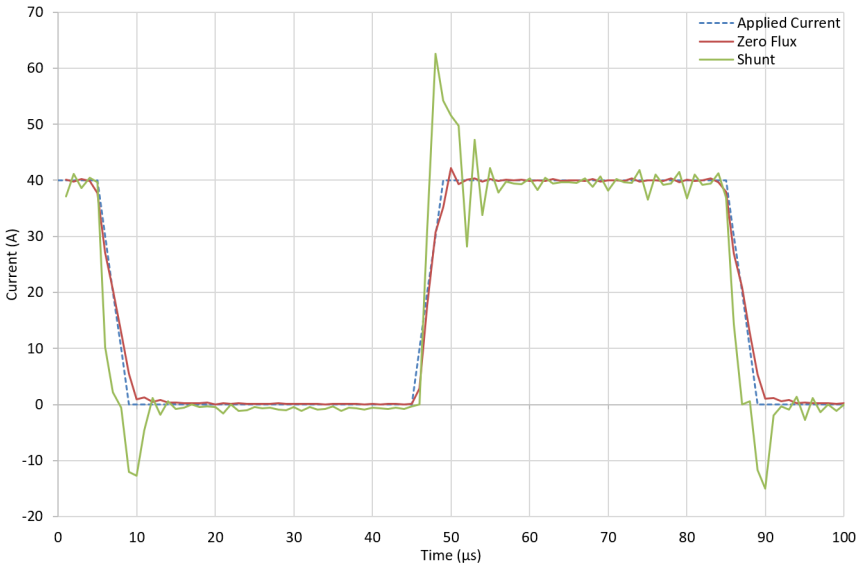

Figure 3.4: Waveform for shunt and zero-flux current sensor (40 A)

The next step was to establish the relation of the current magnitude and the distortion in the measured current.

3.3.2. Duty cycle and time interval

The first test is to analyze the effect of t_{on} and t_{off} along with the current magnitude on the measured current by the zero-flux current sensor. For this, two different types of current waveforms were applied to the system. First, a current with a 50% duty cycle is used, i.e., equal on and off time. As can be observed in (3.5) for 50 A applied current, the measured current is follows the applied current with an overshoot of around 12%. However, when the applied current is increased, the measured current is unable to follow the applied current.

For an applied current of 100 A and 150 A, very different behavior is observed. From 70 A onward, the transducer does not follow the applied current, and bending is visible in the curve. Also, some considerable overshoot is visible, around 20% the applied current. This bending is observed only on the rising edge. The measured current follows the applied current during the falling edge in all three cases. This can imply that the zero-flux can follow the applied current, but another component in the circuit cannot.

Next, increasing the t_{on} and keeping the same time period, the applied current is increased. As can be observed in (3.6) measured current follows the applied current again for 50 A and even for 100 A. But, for measured current is unable to follow the applied current for an applied current of 150 A. For an applied current of 100 A, the measured current has a slow settling time. This may be due to the power supply. The power supply may not be able to follow the chopping of the current.

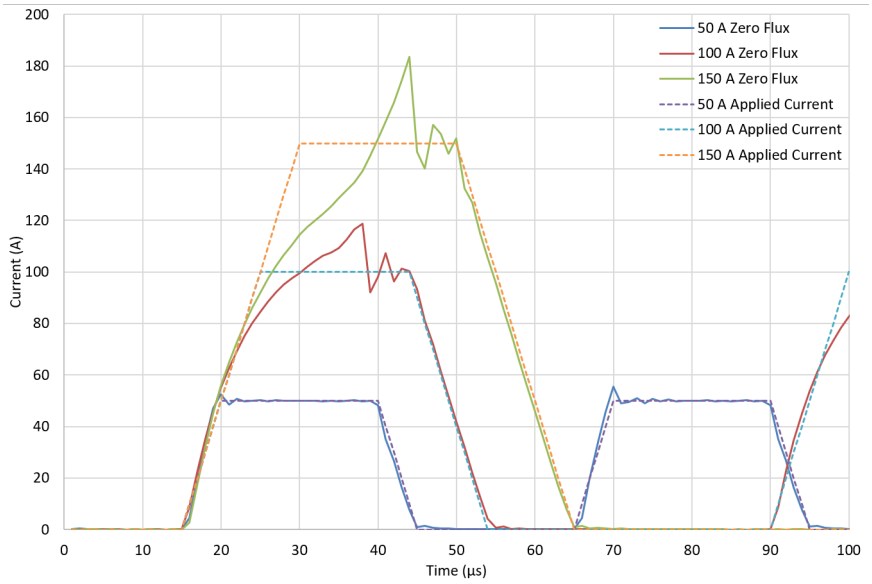

Figure 3.5: Zero-flux current measurement for 50% duty cycle

As per the observation, the current measured by the zero-flux current sensor for 100 A and 150 A cannot follow the applied current. Especially 150 A did not settle at all. It was concluded that the settling time for the higher current was longer than the t_{on}. 100 A current is applied for a longer time interval, and the current measured by zero-flux current sensor settles (3.7). The time interval was further increased for 150 A. But, the current measured by the zero-flux current sensor does not settle (3.8). The measured current follows the applied current till 80 A then has very different behavior. This may be due to the power supply's incapability to follow the switching of the applied chopped current.

3.3.3. Interpolation function

Programmable DC electronic load has an in-built interpolation function. This function can be used to enable or disable intermediate data point estimation. Using this function, we concluded that keeping the interpolation function leads to shorter settling time and less current overshoot (3.9). However, this also leads to a higher slew rate due to additional data points.

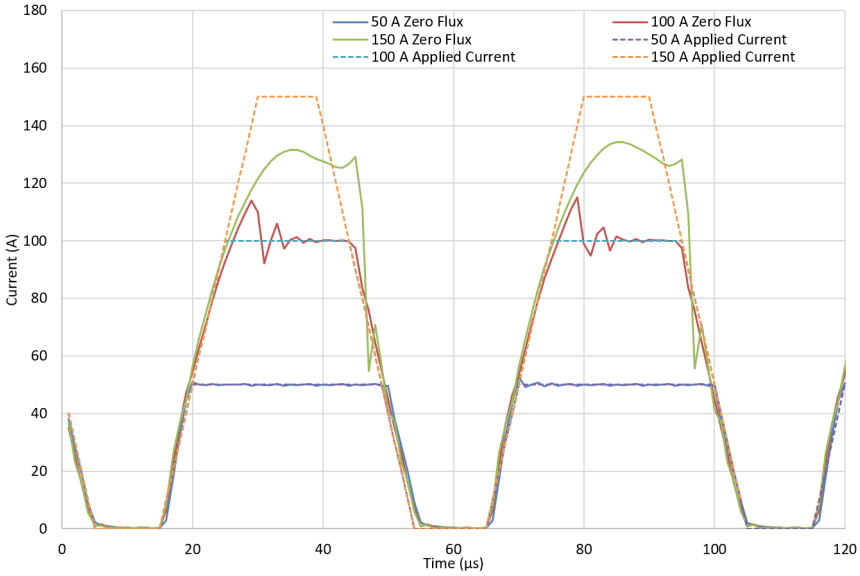

Figure 3.6: Zero-flux current measurement for same time interval

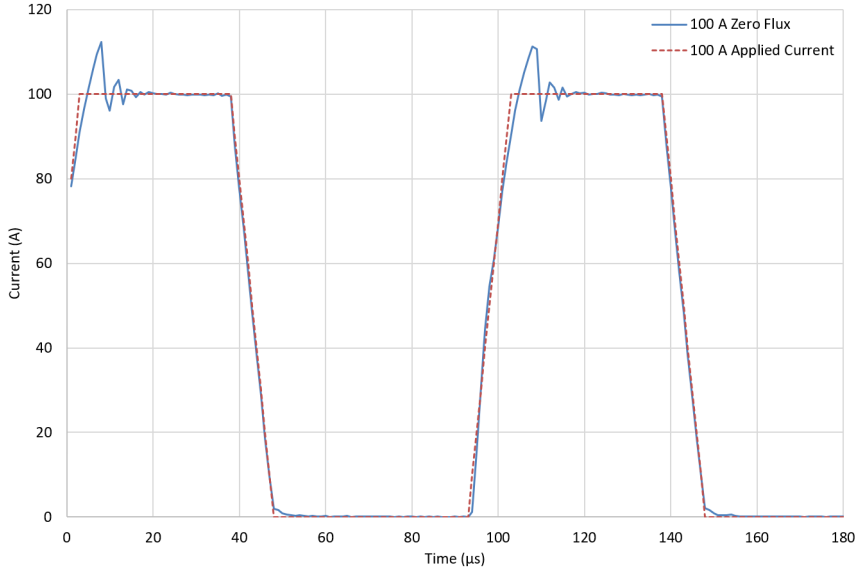

Figure 3.7: Zero-flux current measurement for a longer time interval at 100 A

3.3.4. Interval function

Programmable DC electronic load has an in-built interval function. This function is used to set the interval of the waveform. This changes the resolution of the

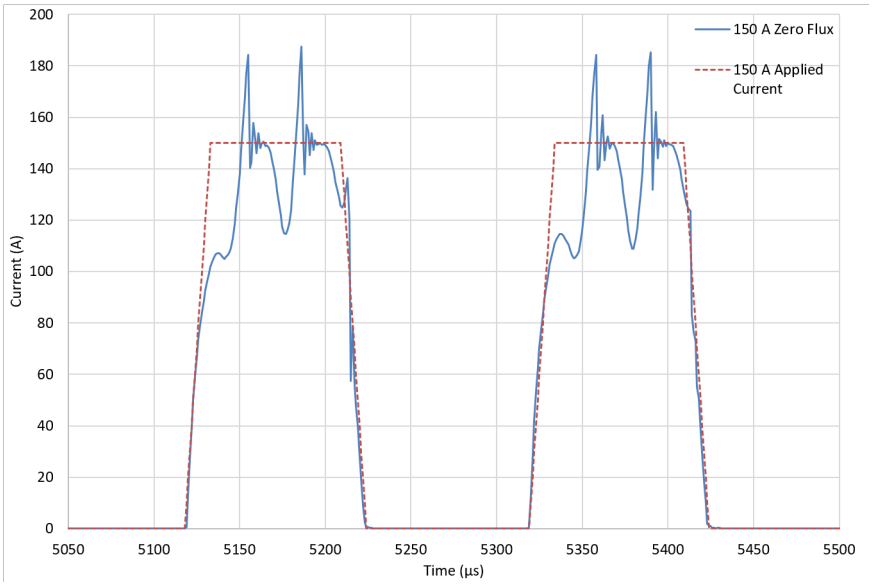

Figure 3.8: Zero-flux current measurement for longer time interval at 150 A

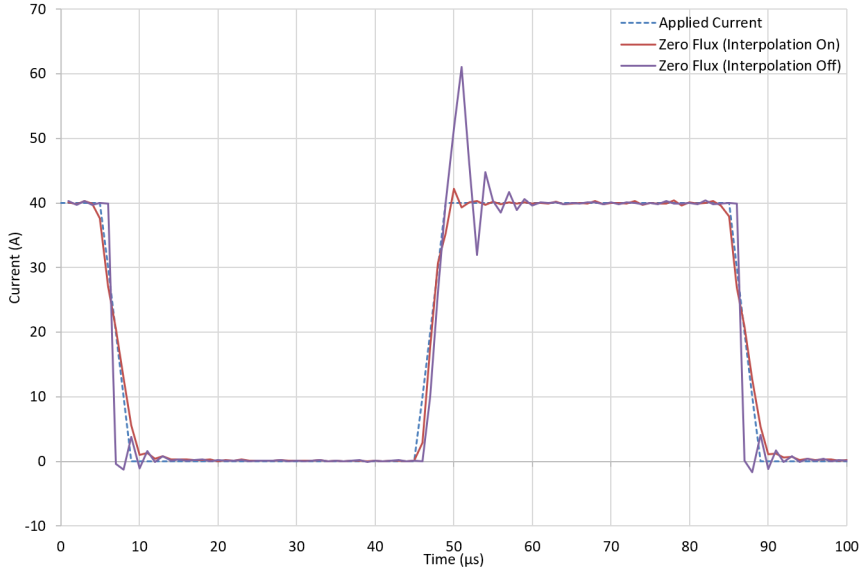

Figure 3.9: Interpolation function for 40 A Zero-flux current measurement

waveform. As can be observed in the graph (3.10), increasing the interval, i.e., increasing the resolution, decreases the settling time and current overshoot.

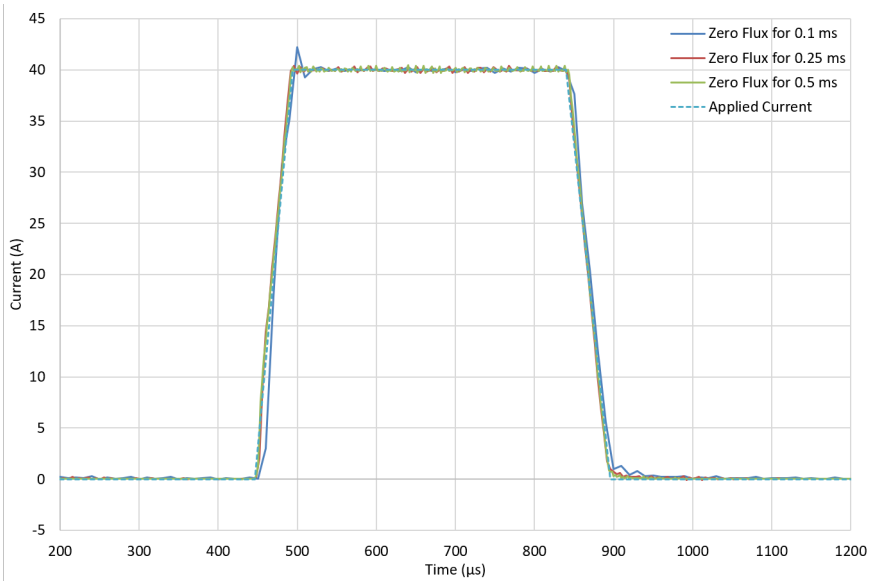

Figure 3.10: Interval function for 40 A Zero-flux current measurement

3.4. Summary of tests

The zero-flux current sensor is more stable and accurate than the shunt, maybe due to heat dissipation in the shunt. The tests performed on the revised test setup (3.3) showed that zero-flux current measurement (reference transducer) could follow the applied chopped waveform to an extent. The overshoot is around 12% for lower applied current. At a higher value of current, the overshoot goes up to 20% of applied current. Increasing the applied current leads to the incapability of the measured current to follow the applied current. Also, this increases the settling time. The interpolation function in the programmable load, when enabled, leads to shorter settling time and small overshoot. Increasing the resolution by increasing the time interval reduces the settling time and overshoot of the measured current.

The next step was to propose, build, and test a modified test setup to eliminate programmable DC electronic load's active behavior.

References

[1] H. E. van den Brom, R. van Leeuwen, and R. Homecker, *Characterization of a reference DC current transducer with AC distortion for railway applications,* in *2018 Conference on Precision Electromagnetic Measurements (CPEM 2018)* (IEEE) pp. 1–2.

[2] H. E. van den Brom, R. van Leeuwen, and R. Hornecker, *Characterization of DC current sensors under distorted conditions for railway applications,* in *2018 IEEE International Conference on Electrical Systems for Aircraft, Railway, Ship*

Propulsion and Road Vehicles & International Transportation Electrification Conference (ESARS-ITEC) (IEEE) pp. 1–6.

[3] H. E. van den Brom, R. van Leeuwen, and R. Hornecker, *Characterization of DC current sensors with AC distortion for railway applications,* in *IEEE Transactions on Instrumentation and Measurement*, Vol. 68, pp. 2084–2090.

4

Modification of test setup

The, active behavior of the high-power DC current source and programmable DC electronic load leads to a distortion in the waveform. Instead of using the electronic load as an active device, we now use it as a passive load to avoid settling times. Two different circuits were suggested, one with a switch and external load other with two switches and two external loads. The switching action of the electronic switch would generate the chopped wave instead of the electronic load.

4.1. Modification option 1

Option 1 (4.1) consists of an electronic switch (Q), an external resistance (R_{ext}) along with the current source and the electronic load. The electronic load is rated for the maximum load current of 600 A. The DC current source is capable of supplying 900 A. At maximum value when the switch (Q) is on, the electronic load consumes 600 A. The remaining 300 A current would flow through the external resistance R_{ext}. When the switch is off, all the 900 A current will pass through the external resistance (R_{ext}) 4.1. Since the maximum voltage provided by the high-power DC current source is 5 V and the maximum current of 900 A. When the switch (Q) is off, all current passes through the external resistance, which results in the value of the external resistance (R_{ext}) as 5.55 $m\Omega$.

MOSFET (Q)	On	Off
Current by high-power DC current source	900 A	900 A
Current through programmable load	600 A	0 A
Current through R_{ext} (5.5 $m\Omega$)	300 A	900 A
Voltage across high-power DC current source	1.65 V	4.95 V

Table 4.1: Current and voltage parameters for modification option 1

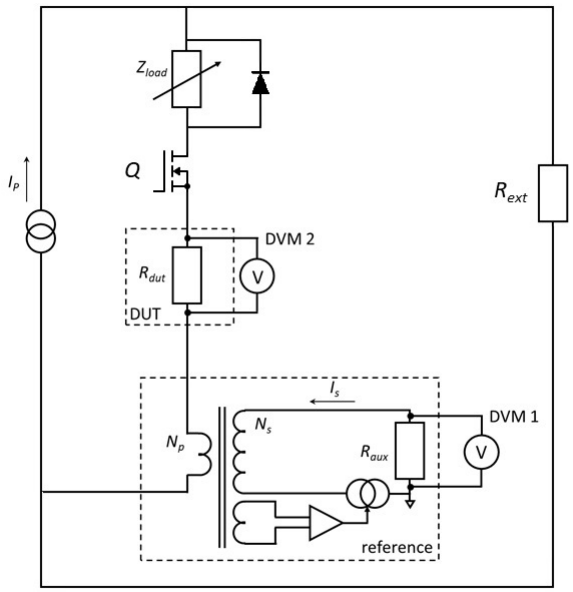

Figure 4.1: Schematic of the modified measurement setup (Option 1)

4.2. Modification option 2

Another option was proposed, which consists of an additional switch and another external resistance beside the ones proposed in option 1. At the maximum source current of 900 A, when the switch Q_1 is on, the programmable load consumes 600 A. The remaining 300 A current flows through the external resistance R_{ext1}. When the switch is off, 600 A current would flow through the external resistance R_{ext2} and the switch Q_2. The remaining 300 A current would continue to flow through R_{ext1} (4.2). This implies that the switching of Q_1 and Q_2 needs to be complementary. Presence of R_{ext1} keeps the voltage across the current source constant as the current through R_{ext1} remains constant throughout the switching operation 4.2.

MOSFET Q_1	**On**	**Off**
MOSFET Q_2	**Off**	**On**
Current by high-power DC current source	900 A	900 A
Current through programmable load	600 A	0 A
Current through R_{ext1} (16.5 $m\Omega$)	280 A	280 A
Current through R_{ext2} (7.7 $m\Omega$)	0 A	600 A
Voltage across high-power DC current source	4.62 V	4.62 V

Table 4.2: Current and voltage parameters for modification option 2

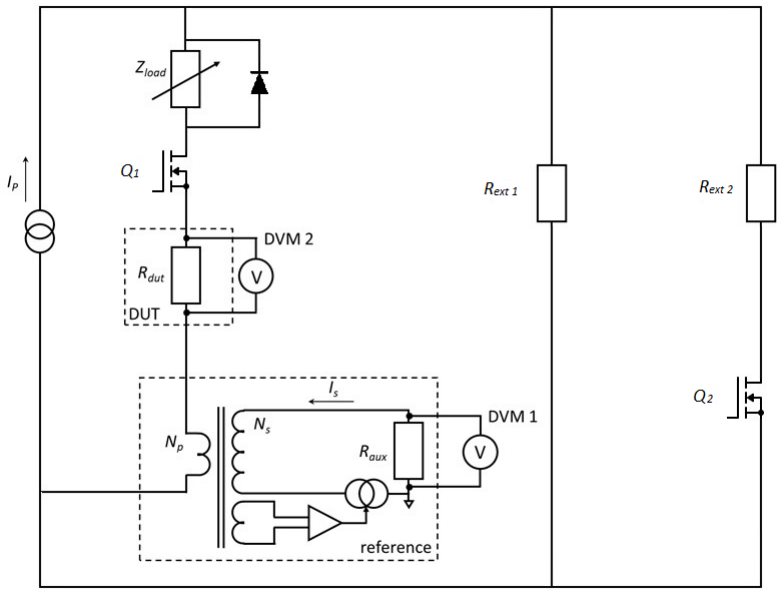

Figure 4.2: Schematic of the modified measurement setup (Option 2)

Option 1 is a simple circuit with one set of resistance and an electronic switch. Whereas, option 2 has two sets of resistance and switch, which would increase the cost of setup and additional heat dissipation. Also, simultaneous switching of Q_1 and Q_2 should be soft switching to order short-circuit. However, the advantage of option 2 to keep the voltage across the current source makes the current source also a passive component. To keep the circuit simple and avoid two sets of resistance and switch, we chose to go ahead with Option 1.

4.3. External resistance

The external resistance (R_{ext}) needs to be rated for 900 A at 5 V. This would be 5.55 $m\Omega$. The resistance should be able to handle the power dissipation of 4.5 kW. This would be a special resistor having low resistance with a high power rating. Several resistance manufacturers were contacted, and various options were explored. Frizlen's steel grid resistor was the best suitable resistor available in the market. It consists of five steel grid plates, each rated at 2.2 $m\Omega$ (4.3a) connected in series internally, this would ensure the net resistance of one set would be 11 $m\Omega$ (4.3). Two of them would be connected in parallel to attain the net resistance value of 5.5 $m\Omega$. This would ensure the power rating of resistance.

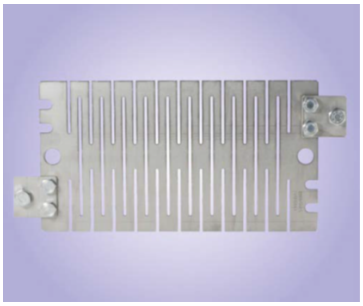

(a) Resistance grid plate of 2.2 $m\Omega$

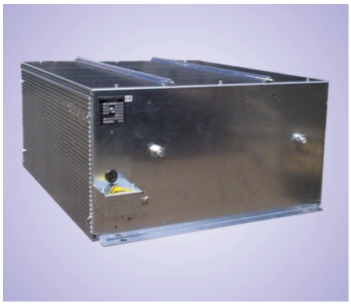

(b) Resistance grid bank of 11 $m\Omega$

Figure 4.3: External resistance rated for high current

4.4. Electronic switch

The semiconductor device for switching needs to be a three terminal device fully controllable to generate the desired fast switching characters tics. The chopped wave has a high switching frequency, which means a continuous operation. For high-current application Field-effect transistor (FET), Insulated-gate bipolar transistor (IGBT) and Integrated gate-commutated thyristor (IGCT) are possible options [1–3]. But, IGCT has high switching losses and therefore typical switching frequency up to 500 Hz, much below the required value of 20 kHz [4]. And, IGBT is capable for high-current application but has high voltage rating [3].

Based on high current capacity and low resistance requirements, field-effect transistors (FETs) were chosen. Metal–oxide–semiconductor field-effect transistor (MOSFET), a type of insulated-gate FET (IGFET), would be suitable as it requires minimal trigger current to control the load current and has minimal internal resistance. The selection criteria are mentioned in 4.3 current carrying capacity In order to handle high current, low resistance N Channel molding type MOSFET module (4.4a) was selected. Queries were sent to number of MOSFET manufacturers and based on options available in the market 4.4, IXYS TrenchT4 Power MOSFET IXTN660N04T4 (4.4b) was selected. Some crucial ratings of this Power MOSFET are discussed in the 4.5.

	Criteria	**Value**
1	Current	600 A
2	On resistance	Very low
3	Voltage drop	Very low
4	Switching frequency	in order of kHz

Table 4.3: Criteria for MOSFET selection

	OEMs	Model	Ratings	Operating conditions	Conclusion
1	IXYS	VMO 1200-01F	V_{DSS}: 100 V I_{D25}: 1200 A $R_{ds(on)}$: 1.25 mΩ R_{th}: 0.065 K/W t_r: 1620 ns	Moderate rise time, suitable for our application. But low thermal resistance cannot be achieved with the passive heat sink. The manufacturer suggests achieving such low thermal resistance using cold plate heat sink with liquid cooling. Not available in stock: The lead delivery time was 24 weeks.	Long delivery time and complicated cooling system: **Not selected**
2	MACMIC	MMN668A010U1	V_{DSS}: 100 V I_{D25}: 688 A $R_{ds(on)}$: 1.25 mΩ R_{th}: 0.14 K/W t_r: 88ns	Low rise time, suitable for our application.	No supplier:**Not selected**
3	Starpower	MD1020SGN100B3S	V_{DSS}: 100 V I_{D25}: 1020 A $R_{ds(on)}$: 1.5 mΩ R_{th}: 0.065 K/W t_r: 272 ns	Low rise time, suitable for our application.	No supplier: **Not selected**
4	IXYS	IXTN660N04T4	V_{DSS}: 40 V I_{D25}: 660 A $I_{L(RMS)}$: 200 A $R_{ds(on)}$: 0.85 mΩ R_{th}: 0.144 °C/W t_r: 430 ns	Low rise time, suitable for our application. Because of the external lead current limit of 200 A, low heat dissipation.	Best possible option, readily available in stock: **Selected**

Table 4.4: MOSFET options

(a) Schematic of N-channel MOSFET

(b) IXYS IXTN660N04T4 MOSFET

Figure 4.4: Power MOSFET selected for switching

As per the ratings of IXTN660N04T4 given in 4.5, the continuous on-state drain current I_{D25} is 660 A; however, the maximum lead current $I_{L(RMS)}$ is 200 A as per the rating. So, it was decided to use four MOSFETs in parallel (4.5) to limit the current through each MOSFET well below $I_{L(RMS)}$. The value of the gate charge (on) $Q_{g(on)}$ is crucial to decide the design of the gate trigger circuit. The gate trigger circuit should be able to provide the four times the gate charge (on) for turning on the MOSFET. If this is not the case, the trigger circuit will not be able to drive the MOSFET, which can cause asynchronous switching of MOSFETs or some MOSFETs not switching at all. In both the scenarios, this may lead to a drain current exceeding $I_{L(RMS)}$ limit. The rise time t_r and the fall time t_f should be small. Other ratings, such as thermal properties, were taken into account to decide the size of the heat sink.

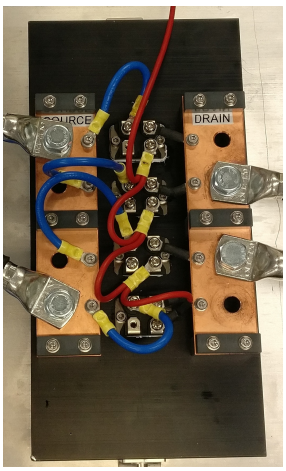

Figure 4.5: 4 MOSFET connected in parallel mounted on Heat Sink

	Rating		Value	Description
1	Power dissipation	P_D	1040 W	Maximum calculated power dissipation by MOSFET based on maximum junction temperature and thermal resistance at (Tc) 25°C case temperature
2	Maximum drain-source voltage	V_{DSS}	40 V	Maximum drain-source voltage without causing an avalanche breakdown with gate-source short-circuited ($V_{GS} = 0$) at 25°C
3	Gate threshold voltage	$V_{GS(th)}$	2-4 V	Gate-source voltage where the drain current starts to flow and the device is considered in on-state
4	Continuous on-state drain current	I_{D25}	660 A	Maximum current rating of MOSFET at a case temperature (Tc) 25°C. Dependent on maximum power dissipation, maximum on-resistance and temperature dependency of the on-resistance. It can be limited by the current handling capacity of the terminal.
5	Maximum lead current	$I_{L(RMS)}$	200 A	Maximum current rating of the MOSFET's lead at 25°C case temperature
6	On-state resistance	$R_{DS(on)}$	0.85 mΩ	On-resistance of power MOSFET, i.e., the resistance between drain to source during on-state. This is the result of source diffusion resistance, channel resistance, accumulation resistance, JFET component resistance, drift region resistance, substrate resistance and bond wire resistance.
7	Input capacitance	C_{iss}	44 nF	Capacitance between the gate and source terminals with $V_{DS} = 0$
8	Output capacitance	C_{oss}	6.5 nF	Capacitance between the drain and source terminals with $V_{GS} = 0$
9	Gate charge (on)	$Q_{g(on)}$	860 nC	Amount of gate charge required to raise the gate-source voltage in order to fully turn-on the MOSFET
10	Rise time	t_r	430 ns	Interval between drain-source voltages from 90% to 10% of its initial value. During this time, the drain current starts to rise and the major part of turn-on losses is generated during this period.
11	Fall time	t_f	260 ns	Interval between drain-source voltages from 10% to 90% of its end value. During this time, the drain current starts to fall and the major part of turn-off losses is generated during this period.

Table 4.5: MOSFET IXTN660N04T4 ratings

4.5. Gate trigger circuit

A gate trigger circuit is required for triggering the MOSFET. Since a single gate driver circuit triggers four MOSFETs, the gate driver chip should simultaneously trigger the MOSFET. Based on our requirements, the IXYS IXD614PI gate trigger chip was selected. The criteria for the selection of the gate trigger are given in the 4.6.

	Rating		Value	Discription
1	Output Voltage	V_O	V_{CC} −0.025 V	The output voltage should be large enough to supply the gate threshold voltage $V_{GS(th)}$ of four MOSFET.
2	Output Current	I_{OUT}	14 A	The gate driver's output current should be large enough to supply four MOSFETs with the flexibility to select gate resistance.
3	Rise time	t_r	50 ns	This rise time should be less than the rise time of the MOSFET so as not to be the limiting factor.
4	Fall time	t_f	40 ns	This fall time should be less than the fall time of the MOSFET so as not to be the limiting factor

Table 4.6: Criteria for selection of gate trigger chip

The next step was to test the trigger circuit and observe the switching effect.

4.5.1. Gate trigger circuit testing

The switching of MOSFET follows the gate signal trigger signal. We use a gate trigger circuit instead of directly connecting the waveform generator for two reasons: Charge required for triggering and protection of the waveform generator. The waveform generator will not be able to provide sufficient gate charges required for switching the MOSFET. The MOSFET requires gate current in the shortest possible time, which cannot be delivered by the waveform generator. During switching, high charge transfer occurs. This may exceed beyond the limit of the waveform generator. The trigger circuit isolates the waveform generator from the MOSFET, which protects it during switching. In the trigger circuit (4.6), 1 Ω resistance is connected at the output of the gate driver chip to increase the rise time and fall time closer to that of the MOSFET.

A test setup was built to analyze the gate trigger circuit's performance (4.6). As the MOSFET is a two-state device, it switches on and off once the desired voltage across the gate-source is reached. The switching behavior follows a square wave pattern even when a chopped wave is the input waveform. Therefore, a square wave from the waveform generator is given as the input to the gate driver circuit. The rise time and fall time were observed for various frequencies and the input

waveform's duty cycle.

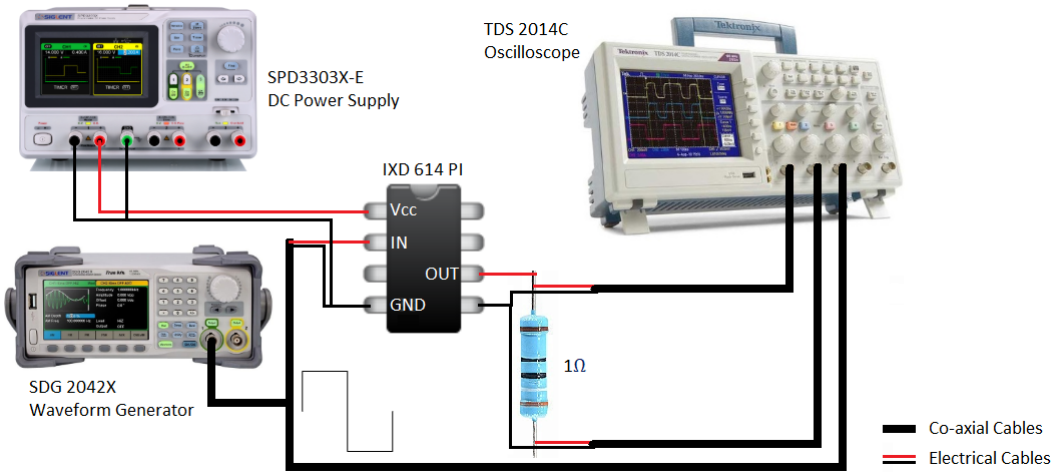

Figure 4.6: Test setup used for testing the gate trigger circuit

The settings for the DC power supply and the waveform generators are as follows:

- DC Power supply

  Voltage to Vcc: 12 V

- Waveform generator 4.7

	Parameters	Values
1	Waveform	Square
2	Frequency	Varied
3	Amplitude	10 V
4	Offset	0 V
5	Phase	0°
6	Duty cycle	Varied

Table 4.7: Parameter settings for the waveform generator

The first analysis was on the rise time and fall time of the output waveform for the frequency of input waveform at 50% duty cycle. It can be observed that the rise time (4.7) and the fall time (4.8) are not significantly impacted by the rise in the frequency of input waveform. The settling time and the overshoot remains the same.

Subsequent analyses are performed on the rise time and fall time of the output waveform for various duty cycles of input waveform at 50 Hz frequency. It was

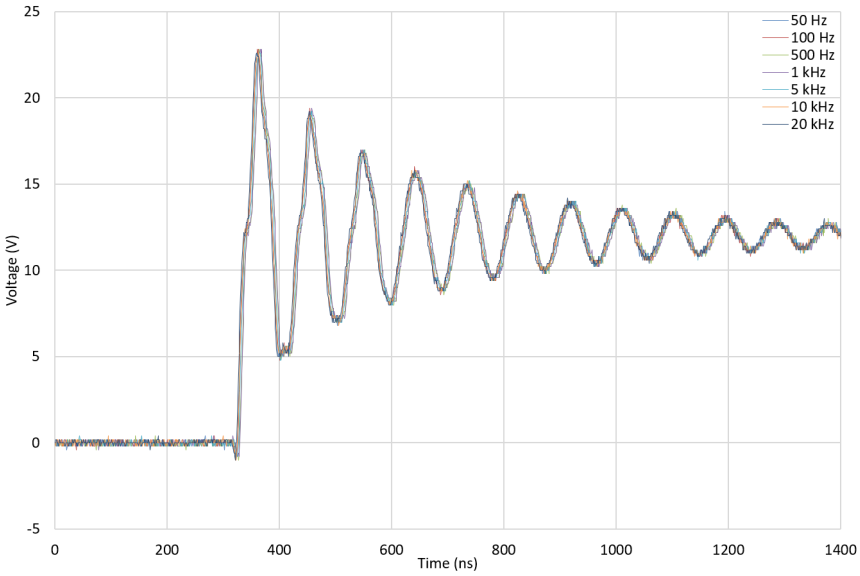

Figure 4.7: Rise time for various frequencies at 50% duty cycle

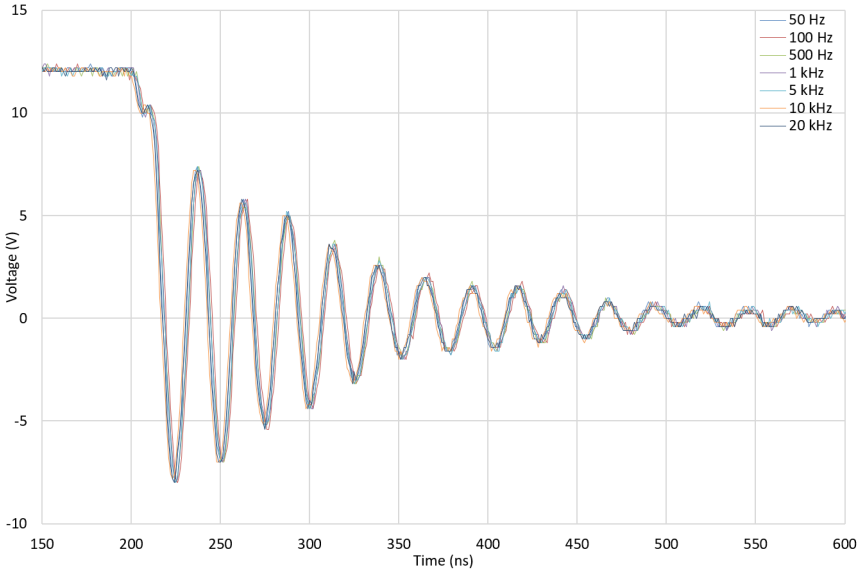

Figure 4.8: Fall time for various frequencies at 50% duty cycle

again observed that the rise time (4.9) and the fall time (4.10) are not significantly impacted by the rise in the duty cycle of the input waveform. The settling time and the overshoot remains the same. The oscillations observed during the tests

(4.7, 4.8, 4.9, 4.10) is expected to dampen when connected to the MOSFET as the internal gate resistance of the MOSFET will be added to the 1 Ω resistance and change the time constant.

These tests verified that the gate trigger circuit is suitable for high-frequency applications and tested up to the required switching frequency of 20 kHz. Any change in the frequency or the duty cycle will not significantly impact the MOSFET triggering and, therefore, on the zero-flux current measurement.

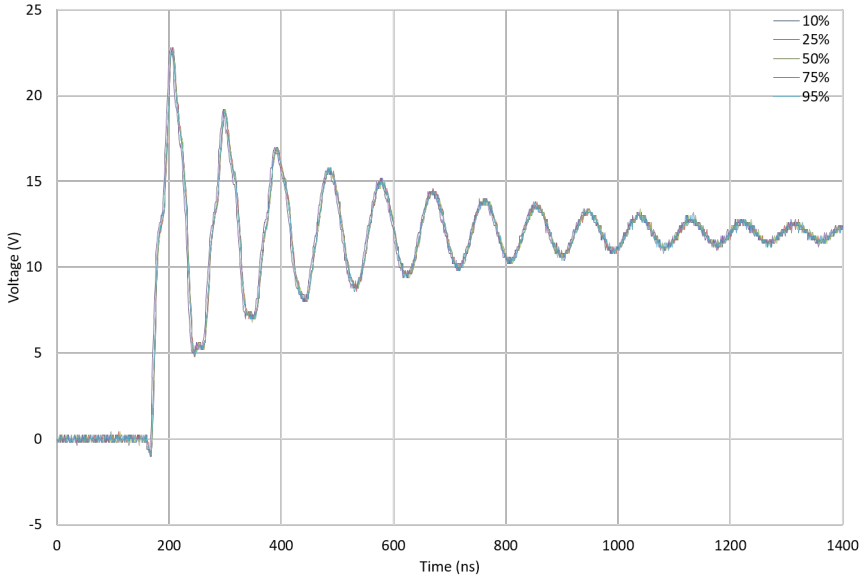

Figure 4.9: Rise time for various duty cycles at 50 Hz

4.5.2. MOSFET testing

After the gate trigger circuit testing, the next step was to test the operation of MOSFET. A simple test setup was realized for MOSFET testing. The objective was to observe the MOSFET triggering and the current distribution in the four MOSFETs. The test setup (4.11) consisted a HP (Agilent) 6672A 0-20 V/0-100 A DC power supply, LEM IT 60-S Ultrastab zero-flux current sensor and Ohm-Labs multiple current shunt. Current through the MOSFET is measured by the voltage across the shunt, zero-flux current sensor, and Fluke 80i-110s AC/DC current probe.

Initially, one MOSFET is tested, and the current supplied by the DC power supply is measured by the current through the shunt. It was observed that the MOSFET is switching as per the expectation, and the current through MOSFET is the applied current. (4.12).

Next, testing of four MOSFETs is carried on by connecting the four MOSFETs in parallel. The current is measured by the voltage across the shunt, zero-flux current sensor, and a current probe. The distribution of current between all the four MOSFETs is approximately 25% each (4.13).

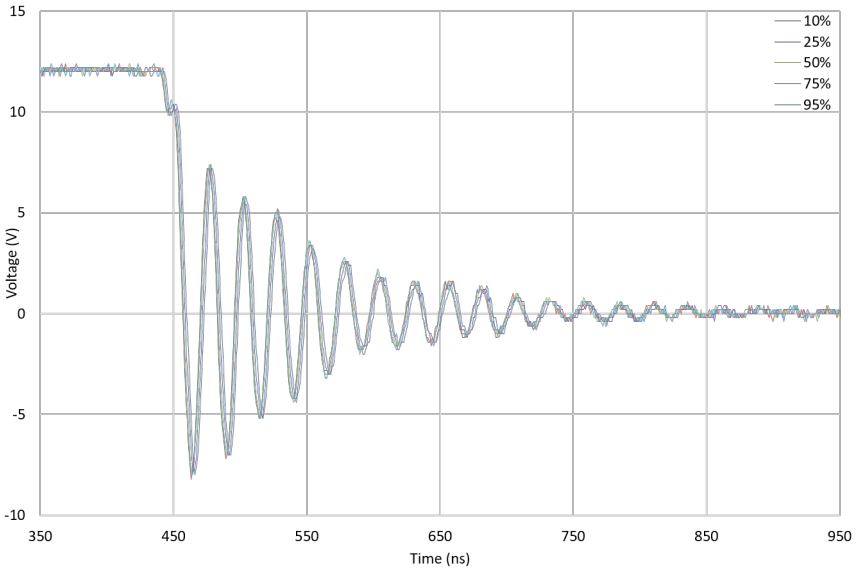

Figure 4.10: Fall time for various duty cycles at 50 Hz

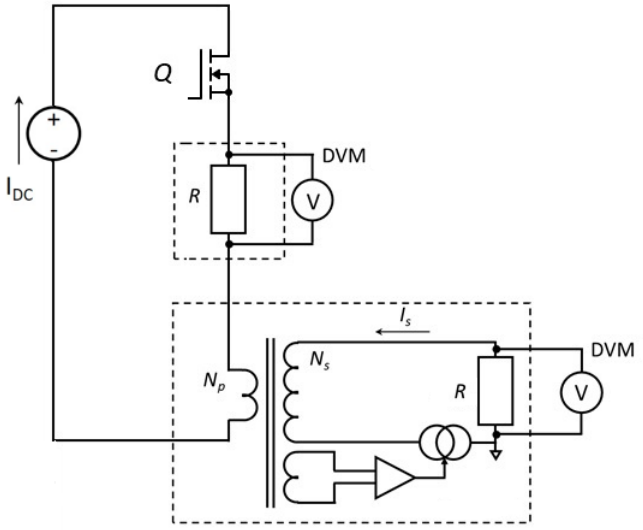

Figure 4.11: Schematic of test setup for MOSFET testing

An interesting and important phenomenon was observed during MOSFET testing. When a chopped waveform is applied as the input waveform to the gate trigger circuit, the MOSFET switching operation was a square wave. This was because the change in MOSFET's state instantaneously when a minimum required number of

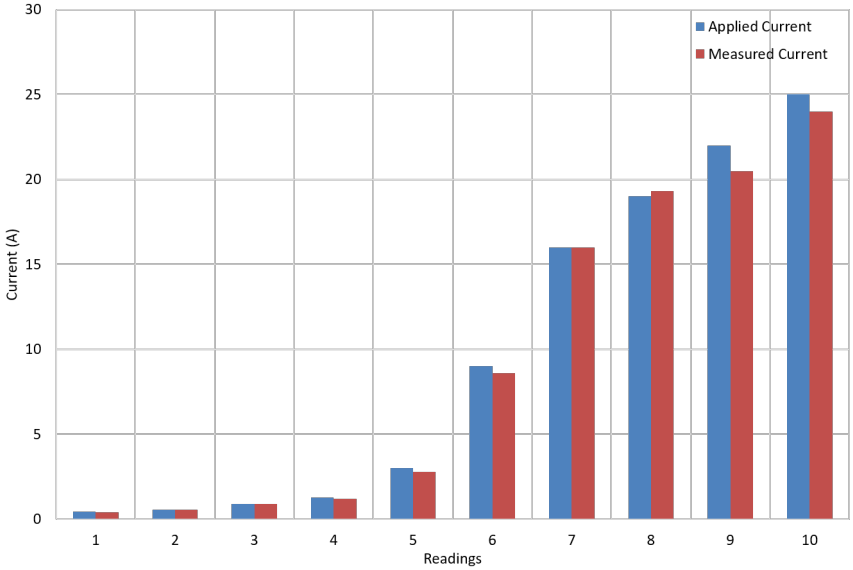

Figure 4.12: Testing of single MOSFET

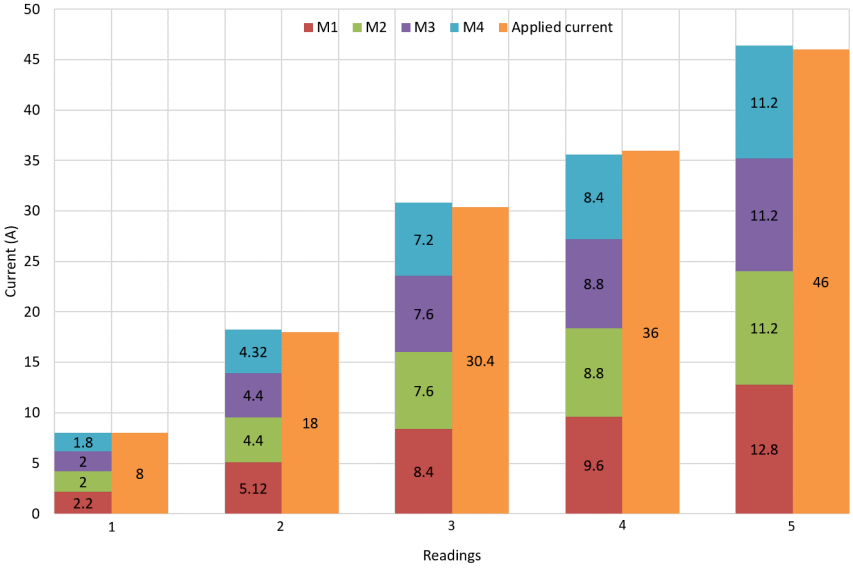

Figure 4.13: Testing of four MOSFETs in parallel

gate charges are supplied to the gate terminal of MOSFET by the gate trigger circuit.

4.6. Diode

A high-current diode is connected in anti-parallel to the programmable DC electronic load. This is connected to provide additional protection to the programmable load during switching of the MOSFETs. When the MOSFETs are turned off, the current through the programmable load is cut-off instantaneously. However, there remains a voltage at the drain terminal of MOSFETs due to the programmable load's power electronic components. The diode provides a path for residual current and reduces the voltage stress across the programmable load. Infineon Technologies diode DZ600N12KHPSA1 rated for average on-state current of 600 A at temperature 100 °C and 735 A at temperature 84 °C.

Figure 4.14: Infineon Technologies DZ600N12KHPSA1 Diode

4.7. Cables

The cable used in the revised setup to characterize the DC shunt current sensor (3.3) had a limitation of 250 A. New cables were required to enable the test at higher current up to 900 A as per the project requirement. Since the signal to be used would be DC with AC distortion in the order of 20 kHz, the cable should be rated for higher current (ampacity). Based on the market availability and discussion with cable manufacturers and vendors, we concluded that a single core cable with an ampacity of 900 A or a multi-core cable would be very thick and rigid to handle, so it was decided to go for multiple runs of small size single core cable. Finally, Top Cable's Marine XTCuZ1-K (AS) low voltage 1×120 mm^2 single core cable was selected. It has open-air ampacity of 333 A at 45 °C, resistance of 0.16 Ω/km at 20 °C and voltage drop of 0.36 V/A.km which is suitable for our application. Two runs for 600 A leg and three runs for 900 A were connected in the circuit.

4.8. Zero-flux current sensor

VSL has already purchased another zero-flux current sensor which is rated up to the primary current of 4000 A. This PM Special Measuring Instrument's Currac 1.0 (4.15) has $I_{primary}$ of 4000 A and $I_{secondary}$ of 1 A. Interestingly; it has tappings at 250 A, 500 A, 1000 A and 2000 A which gives the flexibility for measurement. Also, the opening the head was big enough for two runs of cables selected to pass-through.

Figure 4.15: Zero-flux current sensor rated for 4000 A

4.9. Programmable DC electronic load

As mentioned earlier, the programmable DC electronic load (Chroma 63206A-150-600 rated for 0-150 V, 0-600 A). It can be programmed to simulate various load profiles with uni-polar currents up to 600 A with frequency components up to 20 kHz. It can operate in constant voltage, current, resistance, or power modes to satisfy a wide range of test requirements (4.16).

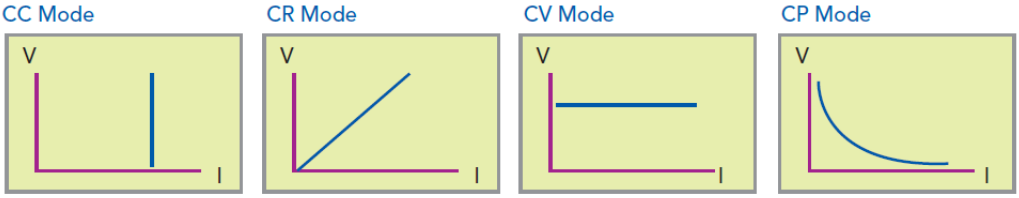

Figure 4.16: Modes of operation of Chroma 63206A-150-600 programmable DC electronic load

4.10. Modified Circuit

To connect the modified circuit, firstly, the two resistance banks of 11 $m\Omega$ connected in parallel with three runs of new cables to get the required 5.5 $m\Omega$ (4.17).

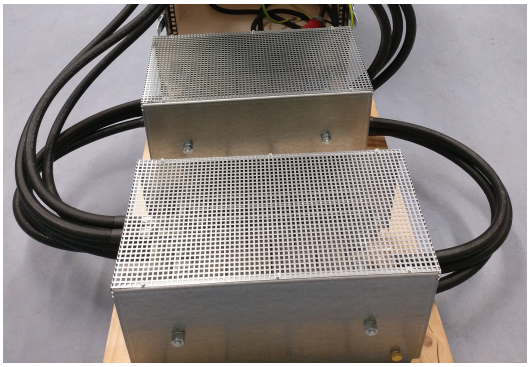

Figure 4.17: Resistance bank of 5.5 $m\Omega$

The current through the programmable DC electronic load and MOSFET would vary between 0 A and 600 A. And the current through the external resistance would vary between 300 A and 900 A. For, 600 A path two-run of cable and for 900 A path three run of cable is required. Additional modifications by copper bus bars were required at the resistance terminals, programmable load terminals, and DC current source terminals for connection of these cables (4.18).

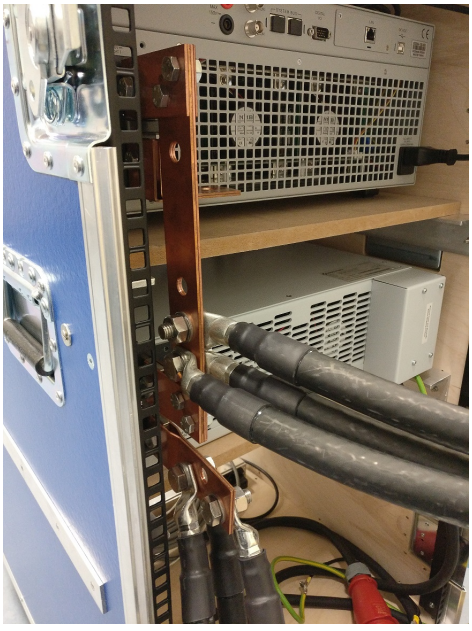

Figure 4.18: Additional copper bus bar for cable connections

Some additional capacitances were added in the gate driver circuit as per the manufacturer's recommendation, which will improve the switching characteristics

by filtering the effect of power supply and MOSFET switching (4.19). The gate driver circuit was developed on a PCB and enclosed in a box with input and output connections (4.20).

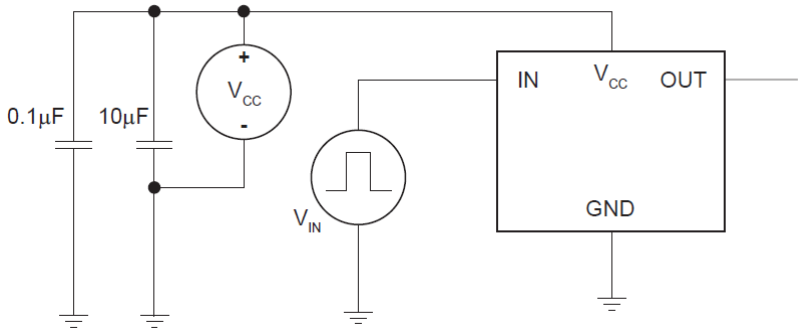

Figure 4.19: Schematic of final gate driver circuit

(a) Input connection for the gate driver circuit

(b) Output connection for the gate driver circuit

Figure 4.20: Gate driver circuit in an enclosure

The final modified test setup (4.21) consists of high-power DC current source, programmable DC electronic load, four parallel MOSFETs, an anti-parallel diode, zero-flux current sensor, and external resistance. The top of the panel has a diode, MOSFET, and zero-flux current sensor (4.22). The panel (4.23) contains programmable DC electronic load (top section of the panel), high-power DC current source (middle section of the panel),and controller for zero-flux current sensor (bottom section of the panel). The waveform generator, power supply for the gate driver, and oscilloscope are kept next to the panel. The external resistance is connected at the rear of the panel with the modified terminals (4.24).

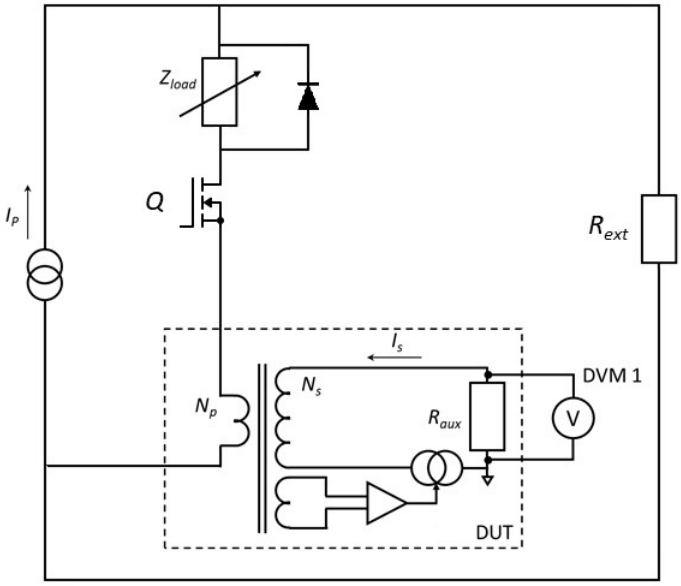

Figure 4.21: Schematic of final modified test setup

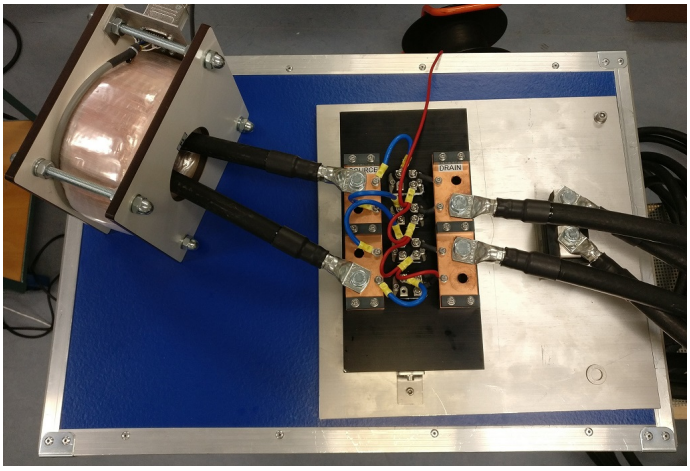

Figure 4.22: Top-view of the final setup

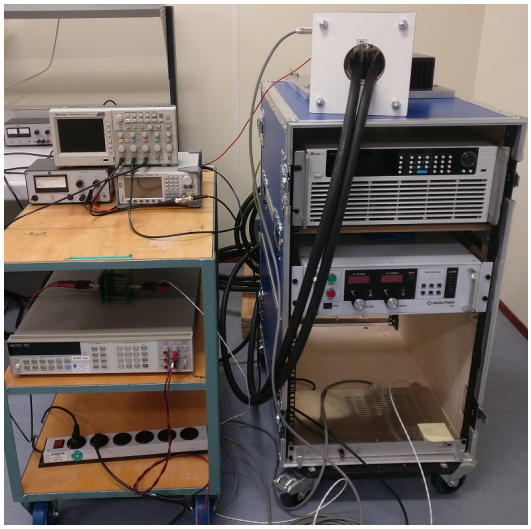

Figure 4.23: Front-view of the final setup

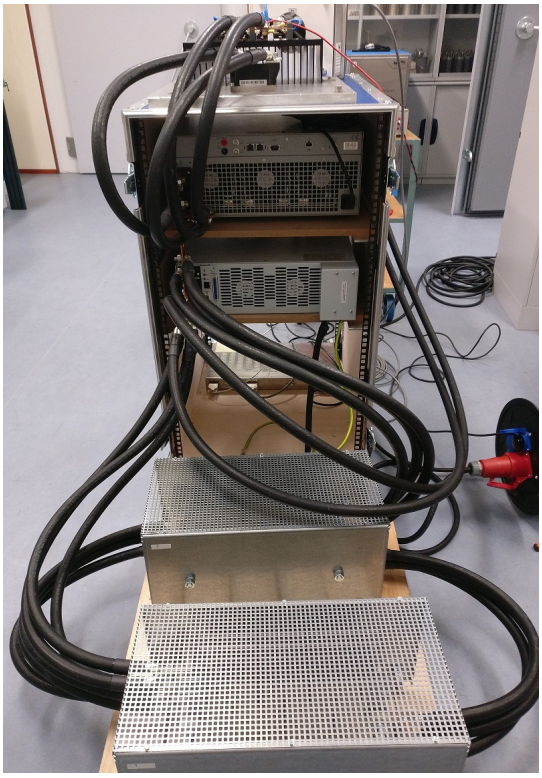

Figure 4.24: Rear-view of the final setup

References

[1] N. Mohan, T. M. Undeland, and W. P. Robbins, *Power electronics: converters, applications, and design*, 2nd ed. (Wiley).

[2] H. Zenk, *Comparison of electrical performances of power electronics switches and an effective switch selection algorithm,* in *Acta Physica Polonica A 2018*, Vol. 133, pp. 897–901.

[3] B. I. Incau, I. Trintis, and S. Munk-Nielsen, *Switching speed limitations of high power IGBT modules,* in *2015 17th European Conference on Power Electronics and Applications (EPE'15 ECCE-Europe)* (IEEE) pp. 1–8.

[4] A. Blinov, D. Vinnikov, V. Ivakhno, and V. Zamaruev, *Hybrid IGBT-IGCT switch,* in *Przegląd Elektrotechniczny 2012*, Vol. R. 88, nr 1a, pp. 12–15.

5

Testing of modified test setup

The modified test setup is now ready for testing. We first start by testing the external resistance and testing the combined testing of the entire test setup. Testing will be divided into continuous operation, i.e., without switching operation and discontinuous operation, i.e., switching operation. The continuous operation would create a constant DC system, which will be used to ascertain the setup's DC characteristic. The discontinuous operation is to simulate the realistic conditions during the regenerative braking action.

5.1. Resistance testing

The rating of one resistance grid bank is 11 $m\Omega$. Two of them connected in parallel are 5.5 $m\Omega$. To test the value of external resistance, an intermediate test setup (5.1) was connected using the high-power DC current source, zero-flux current sensor, and its auxiliaries. Due to the physical constraint, the zero-flux current sensor is placed at the parallel cables between the two resistance banks. So, the current measured by the zero-flux would be half of the current supplied by the high-power DC current source.

$$I_{\text{parallel}} = \frac{V_{\text{measured}}}{R_{\text{aux}}} \times CT_{\text{ratio}} \tag{5.1}$$

$$I_{\text{applied}} = 2 \times I_{\text{parallel}} \tag{5.2}$$

$$R_{ext1} = \frac{V_{R1}}{I_{\text{parallel}}} \tag{5.3}$$

$$R_{ext2} = \frac{V_{R2}}{I_{\text{parallel}}} \tag{5.4}$$

$$R_{\text{ext(measured)}} = \frac{R_{\text{ext1}} \times R_{\text{ext2}}}{R_{\text{ext1}} + R_{\text{ext2}}} \tag{5.5}$$

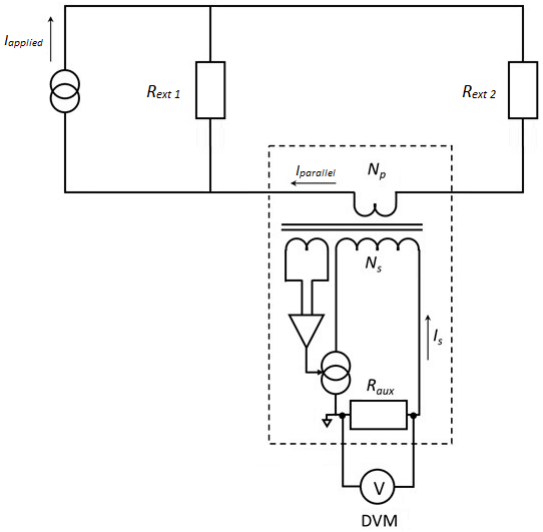

Figure 5.1: Schematic of the test setup for resistance testing

The voltages across of R_{ext1} and R_{ext2} are measured. Based on the current measured using zero-flux current sensor and equations (5.1) (5.3) (5.4); the values of R_{ext1} and R_{ext2} are calculated. Since, R_{ext1} and R_{ext2} are connected in parallel, we use mathematical calculation gives the resultant resistance (5.5). It was observed that the measured value of resistance is well within the tolerance level of ±10% of the designed value (as per the manufacturer).

5.2. Combined testing

This is the final step of testing of the modified setup. In this step, the entire setup is assembled as per the designed circuit (5.2). The first step is to check the setup's working with all components included in the circuit and continuous operation of MOSFET, i.e., 100% duty cycle. The next step is to switch the MOSFET in a square wave pattern. The mode of operation would be varied by input waveform from the waveform generator. Two other quantities can be varied: the current limit, the load current set on the programmable load, and the source current supplied by the high-power current source. Other modes of operation of the programmable load would be explored as per the test requirements. The measured current is calculated using the voltage output by shunt connected to zero-flux (5.6).

$$\text{Measured Current } (I_p) = \frac{\text{Measured Voltage}}{R_{\text{shunt}}} \times \text{Conversion Ratio} \tag{5.6}$$

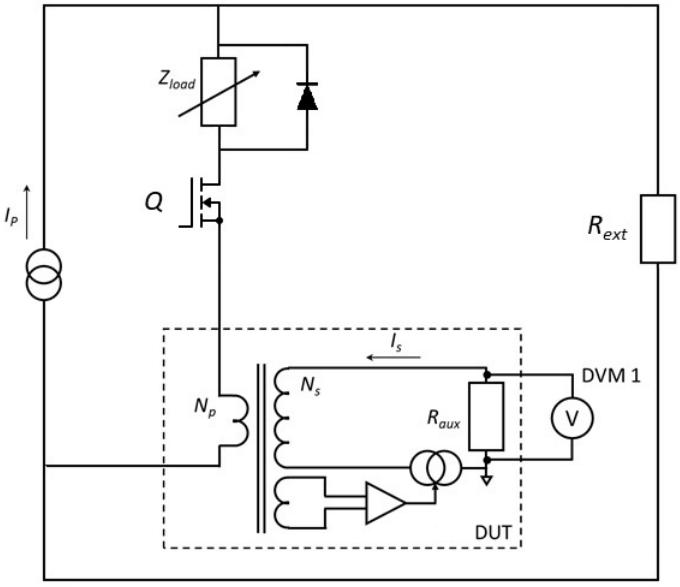

Figure 5.2: Schematic of final modified test setup

5.2.1. Continuous operation

During continuous operation, no switching of MOSFET occurs. MOSFET is set at 100% duty cycle, i.e., always closed. The settings of the waveform generator are listed in 5.1.

	Parameters	**Values**
1	Waveform	Square
2	Frequency	100 Hz
3	Amplitude	10 V
4	Offset	0 V
5	Phase	0
6	Duty cycle	99.99% (maximum possible value, limited by frequency setting)

Table 5.1: Parameter settings for the waveform generator

Constant source current

The programmable load is operated in Constant Current (CC) mode, which means that the programmable load would consume the current set on it manually. The current supplied by the current source is kept constant at 50 A. The load current

is increased step-wise. The zero-flux current sensor measures the current through the programmable load.

At 100% duty cycle, no switching occurs; then, the source's current supply is divided between programmable load and external resistance based on resistance. Based on the current division, the resistance of the programmable load can be calculated. IN CC mode, the minimum resistance value of the programmable load obtained here is 2.93 mΩ. Furthermore, at minimum resistance of 2.93 mΩ, the maximum current through the programmable load is 32.63 A (5.3).

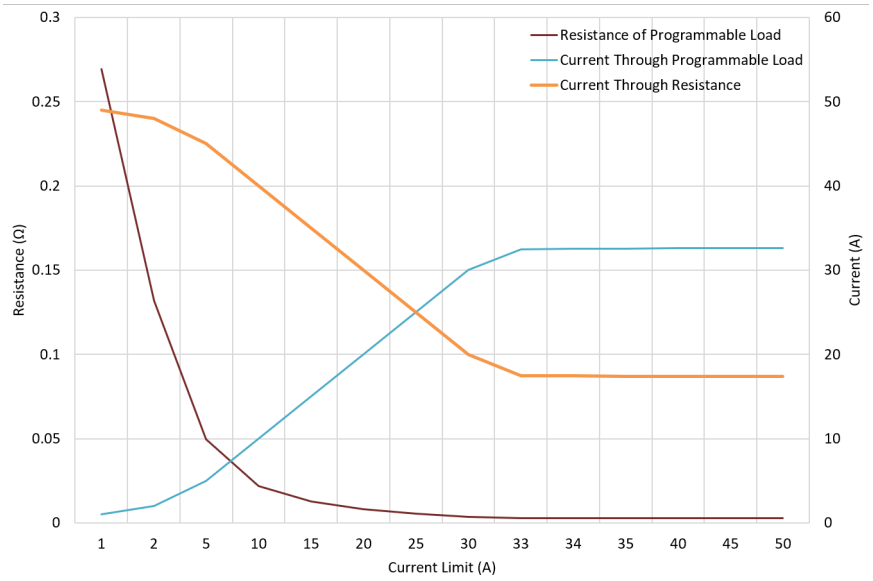

Figure 5.3: Continuous test at 50 A source current in CC Mode

Variable source and load current(CCH Mode)

The programmable load is operated in Constant Current High (CCH) mode. Here, the load current can be set to the maximum value of 600 A. The source current and load current, i.e., the current limit is increased step-wise. The current division between programmable load and external resistance is based on resistance values. It can be observed in the (5.4) that it is close to the linear relation.

Variable source and load current(CR Mode)

The programmable load is operated in Constant Current High (CCH) mode, which means that the programmable load's resistance is constant at the set value. This value is set at the minimum possible value of 5 mΩ, which is also close to the value of external resistance. Since the current division between the external resistance and programmable load is based on the resistance value, the current is approximately equal (5.5).

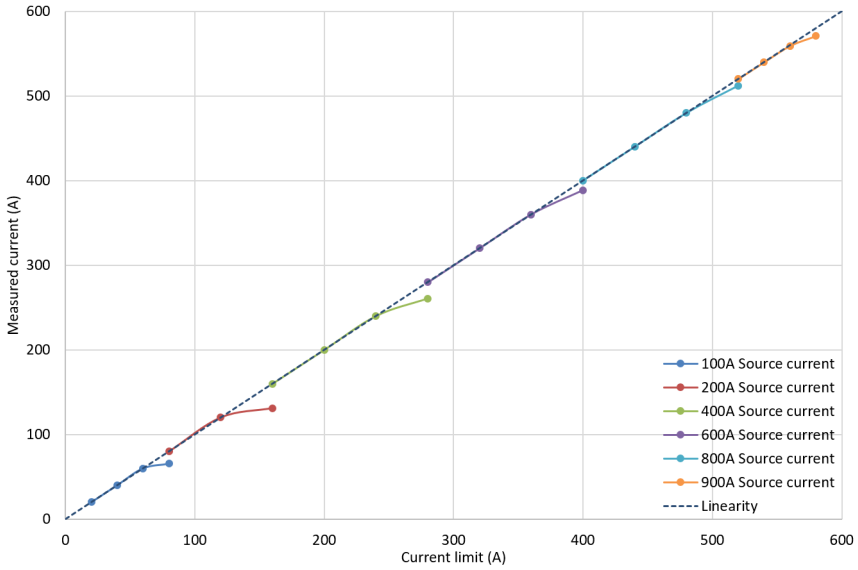

Figure 5.4: Continuous test with variable source and load current in CCH Mode

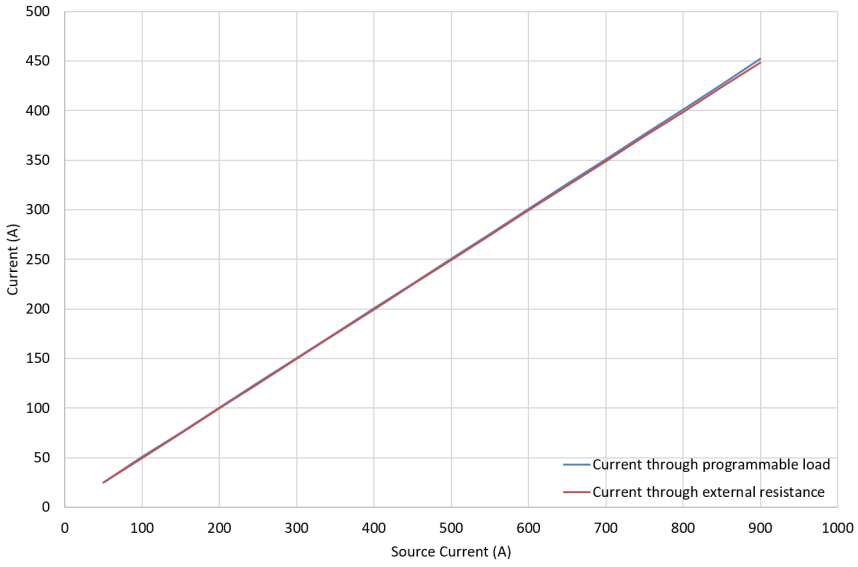

Figure 5.5: Continuous test with variable source and load current in CR Mode

5.2.2. Discontinuous operation

For discontinuous operation, MOSFET switching is controlled by the input waveform of the waveform generator. We tested at a duty cycle of 50%, and the rest of the

parameters remain the same as listed in 5.1. The programmable load in Constant Current High (CCH) mode to ensure constant current operation up to the full capacity of 600 A. The current limit and source current increased step-wise. The terminal voltage of a high-power DC current source is also measured on the oscilloscope.

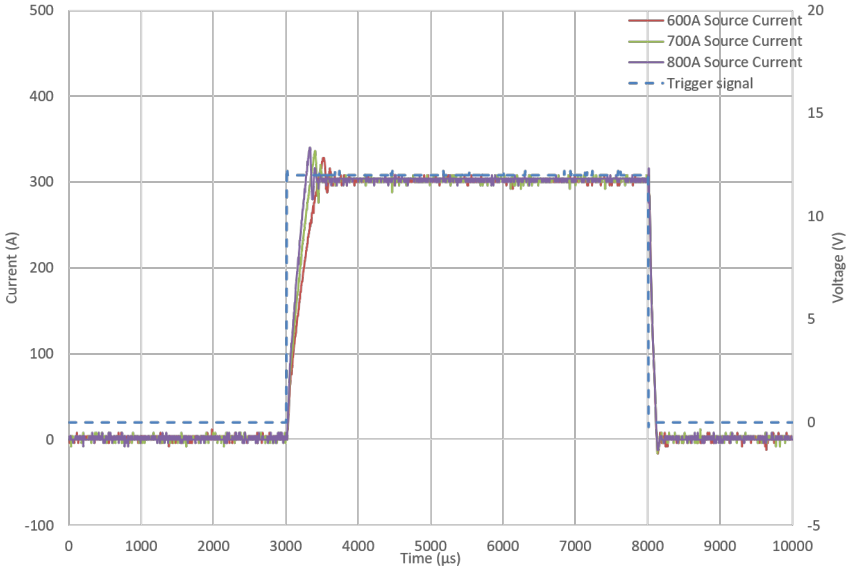

Figure 5.6: Zero-flux current measurement with 300 A current limit and increasing source current

Zero-flux measurement is slow as the current source is not able to follow the trigger signal during turn-on (rise time) (5.6, 5.8). It can also be observed in for current measurement has fast turn-off (fall time). The overshoot decreases with an increase in the current limit and source current. Also, overshoot remains below 20% for load current greater than 100 A. The rise time and settling time reduces with an increase in source current. The terminal voltage of high-power DC current source is slow to follow the switching (5.7, 5.9). During MOSFET turn-off, a voltage spike was observed for source terminal voltage.

5.3. Grounding

In every electrical measurement, the grounding of the system plays an important role. Moreover, grounding is highly critical in a calibration setup. Various grounding connections were realized to analyze the impact of grounding in the current measurement. In the case of improper grounding, oscillations are observed during the turn-off (5.10). The possible reason for distortion may be due to circulating current in case of improper grounding.

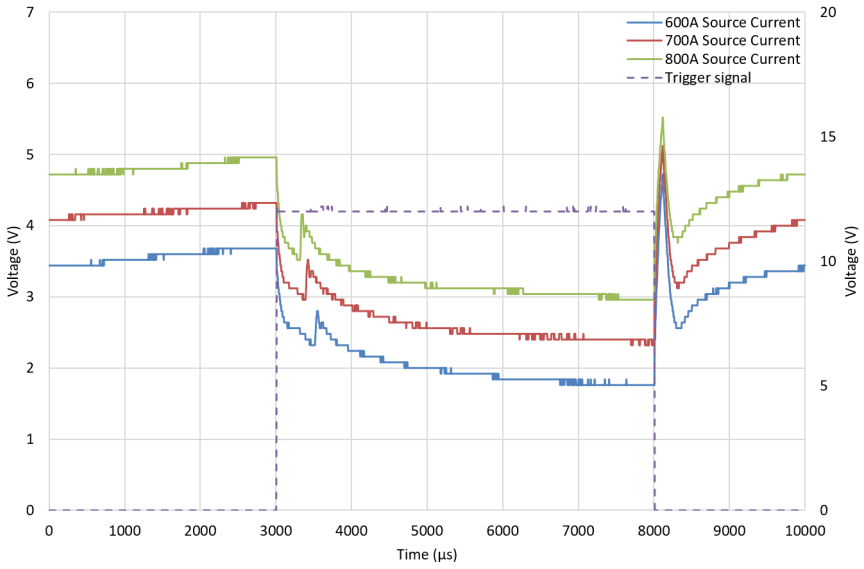

Figure 5.7: Source terminal voltage measurement with 300 A current limit and increasing source current

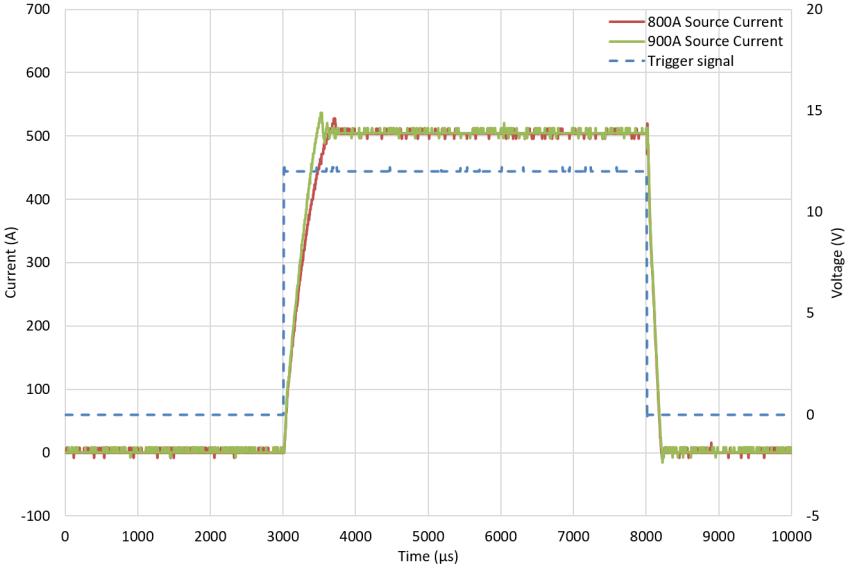

Figure 5.8: Zero-flux current measurement with 500 A current limit and increasing source current

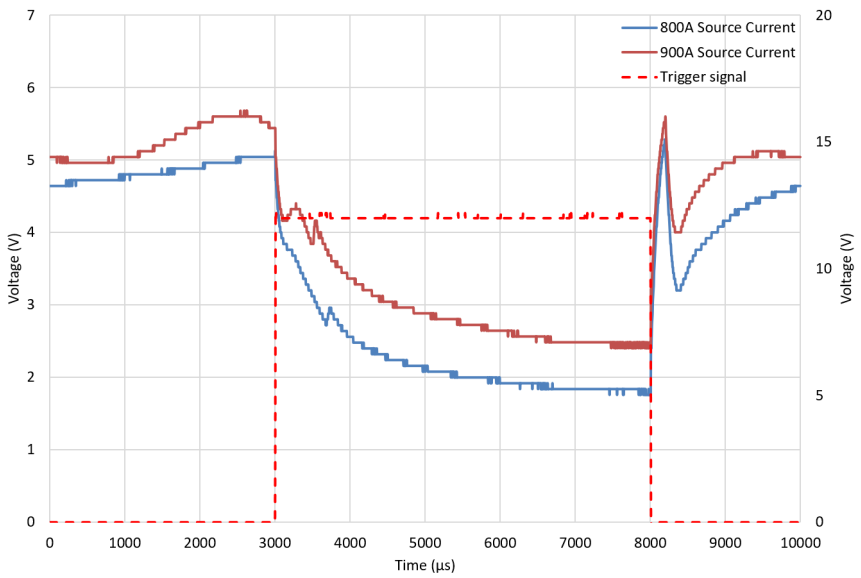

Figure 5.9: Source terminal voltage measurement with 500 A current limit and increasing source current

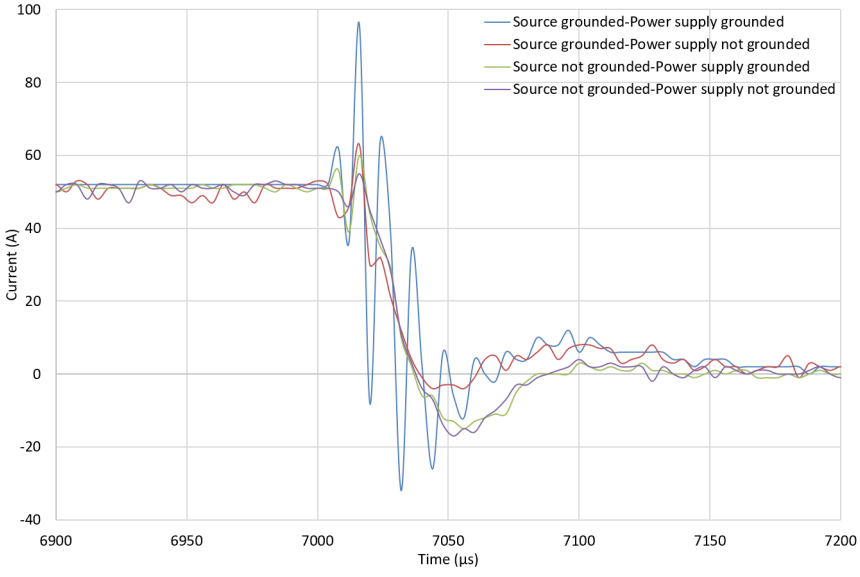

Figure 5.10: Zero-flux current measurement at 50 A current limit and 100 A source current for different grounding connections

5.4. Zero-flux current sensor comparison

A preliminary comparison is performed between the two zero-flux current sensors: LEM ITN 900-S and PM Special Measuring System CURACC 1.0 (4000 A). Due to the physical constraint of the LEM current sensor's opening, only once cable can pass through the opening. Therefore, only one cable is used to connect the source terminal of MOSFET to the current source. The current capacity of a single cable is 333 A as per the manufacturer. However, this is for the continuous current application. The current was limited at 480 A as the heating was observed at the bus-bar connecting the four MOSFETs to the cable.

Less noise is observed for LEM current sensor compared to the LEM current sensor. An analysis of error in current measurement is conducted taking PM zero-flux current sensor as the reference. Using the area under the curve calculation, an average error of 2.79% is calculated. As can be observed from (5.11), noise in PM current sensor may be the cause of this error.

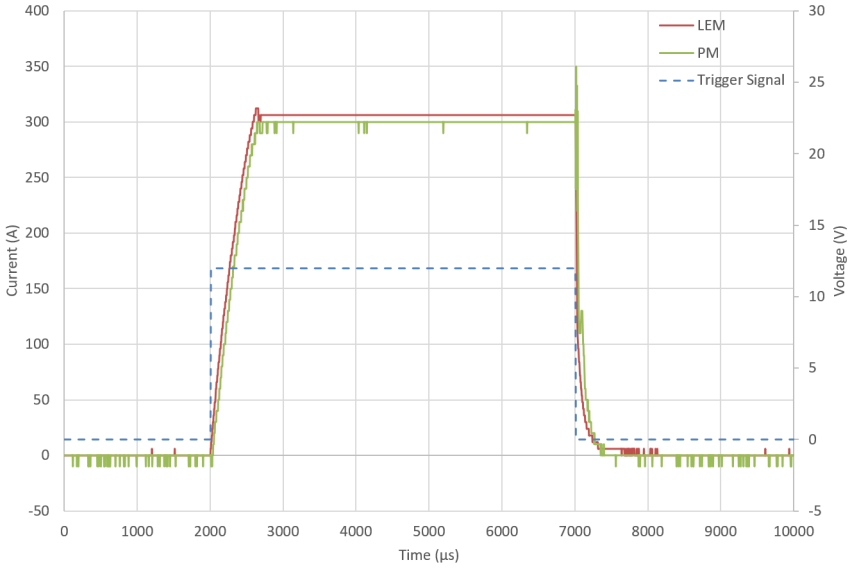

Figure 5.11: Current measurement by LEM and PM zero-flux current sensor for 300 A current limit and 600 A source current

5.5. Uncertainty calculation

Experiments are the basis for the validation of the scientific theory. Moreover, measurement is the quantification of experiments. The incompleteness of measurement results is expressed by estimating the measurement error as the difference between the actual measured value and the "true" value of the measurand [1]. International Bureau of Weights and Measures (BIPM) defines the uncertainty of measurement as a non-negative parameter associated with the result of a measurement that char-

acterizes the dispersion of the values that could reasonably be attributed to the measurand [2].

In our modified setup, the uncertainty due to the current sensor, the shunt, and the oscilloscope voltage measurement contributes to the net uncertainty of the measured current. The current sensors and the shunts are calibrated, and their standard uncertainties are known. The standard deviation is calculated using the DC measurement accuracy of the oscilloscope (5.7). The standard deviation is converted into a standard error, taken here as the uncertainty in the voltage measurement by the oscilloscope.

$$\text{DC measurement accuracy} = \pm\,(3\% \times \text{reading} + 0.1\ \text{div} + 1\text{mV})\ \text{mV} \qquad (5.7)$$

An uncertainty budget is an itemized table of components contributing to the uncertainty in measurement. Here, the uncertainty in current measurement by the zero-flux current sensor, the uncertainty in current to voltage conversion by the shunt, and the uncertainty in voltage measurement by oscilloscope contributes to the combined uncertainty of current measurement 5.2. The combined standard uncertainty for LEM ITN 900-S zero-flux is calculated to be 2.9 ppm and 31.6 ppm for PM 4000A zero-flux. Expanded uncertainty is also calculated using k=2 for 95% confidence interval. The noise observed for PM zero-flux current sensors is the suspected cause for the higher uncertainty.

	LEM ITN 900-S	**PM 4000A**
Source of Uncertainty	**Standard Uncertainty (ppm)**	**Standard Uncertainty (ppm)**
Zero-flux (I)	1.5	0.7
Shunt (R)	1	1
Oscilloscope (V)	2.2	31.6
Combined Standard Uncertainty	2.9	31.6
Expanded Uncertainty (k=2, 95% confidence)	5.7	63.2

Table 5.2: Uncertainty budget for zero-flux current measurement

References

[1] A. Ferrero and S. Salicone, *Measurement uncertainty,* in *IEEE Instrumentation Measurement Magazine 2006*, Vol. 9, pp. 44–51.

[2] International Bureau of Weights and Measures (BIPM), *Guide to the expression of uncertainty in measurement (GUM) 2008,* .

6

Conclusion and future work

The objective of this thesis project was to develop the measurement setup to measure the braking rheostat losses. The energy loss during braking is dependent on the current through the brake rheostat during braking. The initial and revised setup developed earlier at VSL had the following limitations, which formed the research questions (RQ) for this thesis:

1. The distortion in the measured current due to the interaction between the electronic components of the programmable load and the current source.
2. The limitation of load current due to the cable capacity and high settling time at higher current values.
3. The zero-flux measurement does not reflect the intended chopped waveform. This is suspected due to input current not following the ideal chopped waveform. The current source or the programmable load or the circuit is not optimal for high-frequency chopped waveform [1].

The setup was modified after extensive study, and the modified setup was tested in every step. The tests performed on the modified setup lead to some crucial observations that would form the basis for future work and be part of the MyRailS project outcome.

6.1. Conclusion

The previous setup had two active components in the circuit: the programmable electronic DC load and the high-power DC current source. The programmable load was used for switching of the measurand current. The electronic components' interference inside the programmable load and the current source was suspected reason for distortion observed in the current measured by the current sensors.

Also, the zero-flux current measurement was observed not to a chopped waveform. It was concluded that the input current to the circuit is not following the ideal

chopped waveform on further investigation. This may be due to the current source or the programmable load or the complete circuit not ideal for the measurement. Therefore, the test setup was modified by including the MOSFET in the circuit in series with the programmable load and additional external resistance. Programmable electronic DC load is used as a passive component in the circuit (**RQ 1**).

The previous test setup had the current capacity constraint due to cable and programmable load. The cable used earlier had the current carrying capacity of 250 A. So, the tests performed earlier were limited to the circuit current of 250 A. Although the current source was rated to provide current up to 900 A, the previous setup can be restricted to the value of 600 A (the current limit of programmable load) even if the cables are replaced. Therefore, the replacement of cables and the addition of the external resistance extends the current limit of the test setup to fulfill the project requirement of 600 A current measurement (**RQ 2**).

In the previous test setup, the programmable load was responsible for chopping the current to generate a fast-switching chopped waveform. The slew rate of the chopped current was dependent on the switching ability of programmable load. This was limited due to the switching characteristics of the internal electronics of the programmable load and their interaction with the electronic components of the current source. MOSFET in the modified test setup ensures fast switching (short switching time compared to current source). It has also been observed that the settling time and overshoot of the current decreases with an increase in load current and source current values as the current source is unable to follow the trigger signal at low values (**RQ 3**).

In metrology, the measurement results are incomplete unless accompanied by the associated uncertainty of measurement. The current measurement's standard uncertainty was calculated based on three contributing factors: the uncertainty due to current sensors, the uncertainty due to high-precision shunt, and the uncertainty due to voltage measurement by the oscilloscope. Since the current sensors and shunts are calibrated, and their standard uncertainties are known, the standard uncertainty due to voltage measurement by the oscilloscope was derived based on the measurement inaccuracy. Finally, the current measurement's net standard uncertainty is calculated and found to be 2.9 ppm for LEM and 31.6 ppm for PM zero-flux current sensors (**RQ 4**). The higher standard uncertainty for PM zero-flux current sensor is suspected due to noise observed during the current measurement.

The impact of the grounding connection is observed only during the turn-off of the measured current. The rise time can be further reduced by adding the input capacitor parallel to the current source. However, a very high slew rate (short rise time) may lead to higher overshoot. Option 2 (4.2) suggested (with two sets of MOSFET and R_{ext}) might help to reduce the rise time as the voltage and current by the current source would remain constant throughout the current measurement.

6.2. Future work

The noise observed in the PM Special Measuring System CURACC 1.0 (4000 A) is an area of concern. The reason for the noise will be investigated further. The uncertainty of the current measured by the PM zero-flux current sensor is expected

to reduce with a reduction in noise. The addition of the input capacitor may increase the slew rate of the chopped waveform. Finally, the modified system needs to be calibrated with a reference sensor. The calibrated sensor would be used as a reference for calibration of current sensors installed on the train for on-board current measurements.

References

[1] H. van den Brom and R. van Leeuwen, *Calibrating sensors to measure braking chopper currents in DC traction units,* in *2020 Conference on Precision Electromagnetic Measurements (CPEM)* (IEEE) pp. 1–2.

A

Van Swinden Laboratory (VSL)

Van Swinden Laboratatium, commonly known as VSL, is the Dutch measurement standards institute located in Delft, South Holland. VSL is responsible for measurement results of companies, laboratories, and institutions traceable to international standards (SI units). By providing services such as calibrations, consultancy, reference materials, inter-laboratory comparisons, and training courses, VSL makes a vital contribution to the dependability, quality, and innovation of products and processes in commerce and society. VSL is responsible for metrological research and development to improve measurement standards and provide measurement solutions for customers. VSL primarily focuses on the industry and the energy sector.

VSL is a private company with a public task. Based on Article 3 of the Metrology Act, the company has been designated as the Dutch standards institute by Ministerial Decree. First Dutch Innovations is the shareholder of VSL.

VSL deals with the following technologies:

Chemistry	Geometry	Temperature
Pressure	Mass	Time and frequency
Electricity	Light	Viscosity
Ionizing radiation	Flow and volume	Humidity

Van Swinden Laboratory is named after the famous Dutch mathematician and physicist, Jean Henri van Swinden (1746-1823). Van Swinden was part of an international committee to define the meter. Later he applied himself to getting the metric system introduced into the Netherlands. He was also the person who first introduced the meter (a platinum rod) in 1799. The follow-up to this was the Metre Convention of 1875, in which it was agreed at the international level for the first time that countries would start to keep to a single system of weights and measures.

B

MyRailS Project

The proposal's overall objective is to develop the metrological framework and measurement infrastructure that underpin the adoption of energy-efficient technologies in European railway systems. The specific objectives are:

1. To develop a metrological framework comprising laboratory and on-board train calibration/measurement set-ups and robust data processing algorithms (DPA), which allows high accuracy energy and power quality (PQ) measurements under highly dynamic electrical conditions. All major European supply systems (25 kV/50 Hz, 15 kV/16.7 Hz, 3 kV/DC, 1.5 kV/DC, 750 V/DC, and 600 V/DC) are considered.

2. To develop and experiment with a wide-area real-time power quality monitoring architecture, including DPA, PQ indices, and centralized data collection, which allows for both quantifying the efficient use of railway infrastructure and diagnostic studies. Reconcile results against circuit models, including resonance effect at higher harmonic frequencies.

3. To set-up combined measurement-simulation tools that allow the prediction of the impact, in terms of stability and power quality, of new Reversible DC Substations (RSS) on both the railway system and the medium and high voltage (MV-HV) supply grid side. The tools, integrated with real-time eco-driving strategies, shall allow efficient real-time management of power flows and apply to real test cases.

4. To analyze, develop, and implement validated real-time eco-driving algorithms to optimize the speed profile and reduce the energy consumption for a given train journey. To develop set-ups and procedures for traceable measurements of the energy saved by the actual implementation of eco-driving algorithms.

5. To establish a solid database on the evaluation and comparison of railway technologies from the point of view of energy-efficient usage for use by train

manufacturers, railway companies, and standardization organizations. To identify the most promising technologies, practices, and derive implementation strategies for focusing commercialization of the project outputs and further research and development.

B

Project Name		MyRailS			
Project ID		16ENG04			
Website		https://myrails.it/			
Internal Funded Partners		External Funded Partners		Unfunded Partners	
1	INRIM, Italy	7	Comillas, Spain	15	ASTM, Switzerland
2	CMI, Czech Republic	8	HRI, Italy	16	METAS, Switzerland
3	FFII, Spain	9	MM, Spain		
4	LNE, France	10	R.F.I., Italy		
5	NPL, United Kingdom	11	Railenium, France		
6	VSL, Netherlands	12	STRATH, United Kingdom		
		13	SUN, Italy		
		14	Trenitalia, Italy		